



Using Th-U-Pb geochronology to extract crystallization ages of Paleozoic metamorphic monazite contaminated by initial Pb

C.J. Barnes^{a,b,*}, J. Majka^{b,c}, P. Jeanneret^c, G. Ziemniak^{b,d}, E. Kooijman^e, K. Kościńska^b, M. Kielman-Schmitt^e, D.A. Schneider^f

^a Institute of Geological Sciences, Polish Academy of Sciences, Kraków, Poland

^b Faculty of Geology, Geophysics and Environmental Protection, AGH University of Science and Technology, Kraków, Poland

^c Department of Earth Sciences, Uppsala University, Uppsala, Sweden

^d Institute of Geological Sciences, University of Wrocław, Wrocław, Poland

^e Department of Geosciences, Swedish Museum of Natural History, Stockholm, Sweden

^f Department of Earth and Environmental Sciences, University of Ottawa, Ottawa, Canada

ARTICLE INFO

Editor: Dr. Balz Kamber

Keywords:

Scandinavian Caledonides

Monazite

Initial Pb contamination

Pb mobilization

LA-ICP-MS Th-U-Pb isotopic dating

ABSTRACT

Geochronology of Th-rich minerals is advantageous as it allows use of three isotopic systems (i.e., $^{206}\text{Pb}/^{238}\text{U}$, $^{207}\text{Pb}/^{235}\text{U}$, and $^{208}\text{Pb}/^{232}\text{Th}$) for accurate data assessment. The $^{208}\text{Pb}/^{232}\text{Th}$ system is especially advantageous in cases where the dated mineral includes an initial Pb component, as $^{208}\text{Pb}/^{232}\text{Th}$ is the least sensitive to the effects of initial Pb amongst the three systems. This benefit is demonstrated with monazite from a white mica schist of the Tsäkkok Lens, Scandinavian Caledonides, where three distinct generations of Paleozoic monazite (Mnz-I, Mnz-II, Mnz-III) are recognized and dated using laser ablation inductively coupled mass spectrometry. The generations are interpreted to represent monazite crystallization in high-pressure conditions (Mnz-I), followed by lower-pressure monazite growth (Mnz-II), and likely dissolution-reprecipitation of the pre-existing monazite (Mnz-III). The results are compared in Tera-Wasserburg, Wetherill, and Th-U-Pb concordia space for each monazite generation. In both Tera-Wasserburg and Wetherill space, the data are all discordant and indicate an initial Pb component in the monazite. The trend and magnitude of discordance due to initial Pb in Mnz-I and Mnz-II is generally controlled by UO_2 content of the monazite, with higher UO_2 equating to greater radiogenic Pb and a dampening of the initial Pb effect, which is most prominent in the $^{207}\text{Pb}/^{235}\text{U}$ system. For the same generations, initial Pb discordance of $^{206}\text{Pb}/^{238}\text{U}$ versus $^{208}\text{Pb}/^{232}\text{Th}$ is less apparent due to the insensitivity of $^{208}\text{Pb}/^{232}\text{Th}$. Mnz-III does not follow the initial Pb trends, likely due to disturbance of the chemical and isotopic systems during recrystallization. Additional discordance in Mnz-I and Mnz-II, which is not related to initial Pb, is recognized and increases with actinide content. The additional discordance may be due to Pb-mobilization in Mnz-I and Mnz-II domains and is revealed when utilizing the $^{208}\text{Pb}/^{232}\text{Th}$ system due to its insensitivity to initial Pb effects. Consequently, relying only on the U-Pb systems can lead to significant initial Pb overcorrections in Tera-Wasserburg or Wetherill concordia space and to calculations of erroneously young concordia dates. The Th-U-Pb concordia method, incorporating all three systems, does not require an initial Pb correction and, therefore, can account for the additional discordance. The Th-U-Pb concordia dates are interpreted as accurate crystallization ages for Mnz-I (484.7 ± 1.1 Ma, MSWD: 1.4) and Mnz-II (474.7 ± 1.2 Ma, MSWD: 1.9). The timing for Mnz-III formation is not well-resolved as it formed via result of dissolution-reprecipitation of the pre-existing monazite, likely under lower amphibolite- to greenschist-facies conditions.

1. Introduction

Monazite is an important Th-rich mineral used as a tool in geochronology for dating tectonic processes. It is ubiquitous in felsic

rocks, is stable over a very wide range of pressure-temperature (P-T) conditions and can preserve chemically-distinct domains that record multiple stages in a rock's history (e.g., Pyle and Spear, 2003b; Kohn et al., 2005; Finger and Krenn, 2007; Janots et al., 2008; Majka et al.,

* Corresponding author at: Institute of Geological Sciences, Polish Academy of Sciences, Kraków, Poland.

E-mail address: cjbarnes063@gmail.com (C.J. Barnes).

<https://doi.org/10.1016/j.chemgeo.2021.120450>

Received 4 May 2021; Received in revised form 19 July 2021; Accepted 20 July 2021

Available online 24 July 2021

0009-2541/© 2021 The Authors. Published by Elsevier B.V. This is an open access article under the CC BY license (<http://creativecommons.org/licenses/by/4.0/>).

2012; Holder et al., 2015; Skipton et al., 2016; Engi, 2017; Kooijman et al., 2017). The incorporation of Th and U into its structure allows for three isotopic decay systems ($^{208}\text{Pb}/^{232}\text{Th}$, $^{206}\text{Pb}/^{238}\text{U}$, and $^{207}\text{Pb}/^{235}\text{U}$) to be utilized for geochronological analysis (Engi, 2017; Vermeesch, 2020). Although some studies have taken advantage of the $^{208}\text{Pb}/^{232}\text{Th}$ decay scheme (e.g., Schneider et al., 1999; Catlos et al., 2002; Rasmussen and Muhling, 2007; Kohn and Vervoort, 2008; Catlos and Miller, 2016; Jeanneret et al., 2017; Seydoux-Guillaume et al., 2019), reliance on just the two U—Pb systems is common with monazite geochronology (e.g., McFarlane and Harrison, 2006; Moussallam et al., 2012; Kirkland et al., 2016; Skipton et al., 2016; Mohammadi et al., 2019; Yan et al., 2020), because of either preferences in data processing, or analytical/methodological deficiencies. Utilizing the $^{208}\text{Pb}/^{232}\text{Th}$ system is beneficial as it reduces the reliance on the imprecise $^{207}\text{Pb}/^{235}\text{U}$ ratio and is not affected by intermediate daughter product disequilibrium as is present in the U—Pb systems (Schärer, 1984; Parrish, 1990; Anczkiewicz et al., 2001). Moreover, it is relatively insensitive to initial Pb contamination and is therefore less dependent on a ^{204}Pb correction (Vermeesch, 2020) that can be compromised by ^{204}Hg interferences and imprecise measurements with laser ablation inductively coupled mass spectrometry (LA-ICP-MS; Petrus and Kamber, 2012; Schoene, 2014).

The effects of initial Pb are generally not considered for $^{208}\text{Pb}/^{232}\text{Th}$ in monazite as it is widely assumed that monazite does not incorporate initial Pb during crystallization, despite few critical studies investigating initial Pb in monazite since the seminal work of Parrish (1990). This assumption could be important for the Th-U-total Pb dating method (e.g., Suzuki et al., 1991; Montel et al., 1996; Williams et al., 2007; Suzuki and Kato, 2008; Williams et al., 2017; Konečný et al., 2018), which cannot independently assess the three isotopic decay systems, as initial Pb would produce anomalously older dates (e.g., Spear et al., 2009). However, a growing number of studies demonstrate examples of initial Pb contamination of monazite in igneous rocks (Copeland et al., 1988; Kohn and Vervoort, 2008; Catlos and Miller, 2016), associated with ore deposits (Kempe et al., 2008; Krenn et al., 2011), in hydrothermally altered rocks (Janots et al., 2012; Didier et al., 2013), and in metamorphic rocks (Holder et al., 2015; Skrzypek et al., 2017; Jastrzębski et al., 2020). Furthermore, monazite is generally thought to be resistant against Pb-loss due to diffusion in temperature regimes cooler than $\sim 800^\circ\text{C}$ (Kamber and Moorbath, 1998; Cherniak et al., 2004) and does not accumulate significant levels of radiation damage, which would enhance Pb diffusion (Meldrum et al., 1998; Seydoux-Guillaume et al., 2003; Ruschel et al., 2012; Nasdala et al., 2018; Seydoux-Guillaume et al., 2018a; Nasdala et al., 2020). Recent studies have demonstrated that Pb can migrate within the monazite crystal lattice to form Pb nanoclusters (Fougerouse et al., 2018; Seydoux-Guillaume et al., 2019), and that recrystallization of monazite during deformation can also cause Pb mobilization (Erickson et al., 2015). The growing documentation of both initial Pb contamination and the ability for Pb to migrate within the crystal lattice requires greater attention for calculating monazite crystallization ages from large datasets, which stresses the need to develop the utilization of the three isotopic systems (Vermeesch, 2020).

In this contribution, we examine three generations of monazite that formed in eclogite- to greenschist-facies conditions from the Tsäkkok Lens, Scandinavian Caledonides, which records maximum P-T conditions of 2.47 ± 0.32 GPa and $620 \pm 60^\circ\text{C}$ (Bukała et al., 2020). LA-ICP-MS isotopic data are assessed using the traditional Tera-Wasserburg and Wetherill concordia diagrams, and the Th-U-Pb concordia space of Vermeesch (2020). Results of the three methods are compared in terms of precision and accuracy and it is demonstrated that the Th-U-Pb concordia space is superior for Th-rich monazite due to the relative insensitivity of $^{208}\text{Pb}/^{232}\text{Th}$ to initial Pb contamination compared to $^{206}\text{Pb}/^{238}\text{U}$ and $^{207}\text{Pb}/^{235}\text{U}$ in monazite with high Th/U (e.g., Kohn and Vervoort, 2008). Consequently, detection of subtle disturbances of the isotopic systems that are not related to initial Pb can also be detected and addressed. These subtle disturbances are otherwise masked by the higher sensitivity of the U—Pb systems to initial Pb contamination,

which may result in overcorrection of the data and erroneously young crystallization ages (Andersen, 2002; Buick et al., 2006; Corfu, 2013).

2. Geological background

The Tsäkkok Lens, together with the Sarek and Vaimok lenses (Fig. 1), represent the portion of the Seve Nappe Complex (SNC) in the southern Norrbotten county of Sweden. The SNC traditionally represents the outermost portions of the extended Baltica passive margin (Andréasson et al., 1992; Jakob et al., 2019; Gee et al., 2020; Kjöll, 2020). Nappe stacking of the Tsäkkok Lens and other SNC units was the result of the Scandian continental collision between Baltica and Laurentia (e.g., Gee et al., 2008, 2020). The Tsäkkok Lens comprises metasedimentary rocks that host eclogitic bodies. The eclogites record a cold subduction evolution, progressing through blueschist- to eclogite-facies, with conditions of eclogite-facies metamorphism that have been independently confirmed by two studies with conditions of ~ 2.4 GPa and $620 \pm 60^\circ\text{C}$ (Bukała et al., 2020), and $2.5\text{--}2.6$ GPa and $590\text{--}664^\circ\text{C}$ (Fassmer et al., 2021). Garnet Lu—Hf geochronology, conducted using eclogitic samples, has dated prograde metamorphism in the lens to 487.7 ± 4.6 Ma to 484.6 ± 4.5 Ma (Fassmer et al., 2021). Furthermore, eclogite-facies metamorphism was resolved at 481.9 ± 1.1 Ma by means of dilution-thermal ionization mass spectrometry (ID-TIMS) geochronology of zircon extracted from eclogite (Root and Corfu, 2012). The majority of the structures (F2 and S2) preserved in the metasedimentary rocks are related to exhumation of the lens, although a subduction-related foliation (S1) is locally preserved in proximity to eclogitic bodies (Barnes et al., 2020a). In-situ white mica $^{40}\text{Ar}/^{39}\text{Ar}$ geochronology of the metasedimentary structures resolve cooling of the lens at 477.2 ± 4.1 Ma to 475.3 ± 3.5 Ma (Barnes et al., 2020a) after near-isothermal decompression (Kullerød, 1987; Snijlsberg, 1987). Later-stage, noncoaxial deformation of the lens is thought to have occurred during Scandian thrusting in greenschist-facies conditions, beginning at a maximum of c. 423 Ma (Barnes et al., 2020a). The sample (TS17-27; $67^\circ 08' 55.14''\text{N}$ $16^\circ 45' 24.94''\text{E}$) that is the subject of this study is a white mica schist with locally preserved S1 that was folded on the cm-scale into F2 with weak axial-planar S2 foliation development. In-situ white mica $^{40}\text{Ar}/^{39}\text{Ar}$ geochronology was conducted on this sample by Barnes et al. (2020a), yielding single crystal dates that spanned from 487.5 ± 7.3 Ma to 459.1 ± 6.0 Ma. The Tsäkkok Lens in general was deformed during the Scandian event at $\leq 429.9 \pm 9.0$ Ma (Barnes et al., 2020a).

3. Analytical methods

3.1. Electron microprobe analysis

A polished $30\text{ }\mu\text{m}$ thin section was made for electron microprobe (EMP) analysis using a JEOL JXA8230 electron microprobe located at AGH University of Science and Technology (Kraków, Poland), and a JEOL JXA8530F EMP at Uppsala University (Uppsala, Sweden). Images of the general mineral assemblages, and of monazite specifically, were obtained with back-scattered electron (BSE) imaging. A total of seventeen monazite grains were analyzed (Mnz-1 – Mnz-17). Wavelength dispersive (WDS) X-ray chemical mapping of monazite for elements Ca, Th, U, Y, Al was conducted using an accelerating voltage of 15 KeV and beam current of 100 nA and a dwell time of 100 ms. WDS analysis of rutile inclusions in monazite was conducted for Zr-in-rutile thermometry (Zack et al., 2004; Ferry and Watson, 2007; Kohn, 2020). A $1\text{ }\mu\text{m}$ beam diameter was used with an accelerating voltage of 15 KeV and beam current of 120 nA. Oxide weight percentages were obtained for V_2O_5 , Nb_2O_5 , SiO_2 , TiO_2 , ZrO_2 , Al_2O_3 , Cr_2O_3 , and FeO.

3.2. Monazite trace element analysis and Th-U-Pb geochronology

Trace element and Th-U-Pb analyses in monazite were performed in

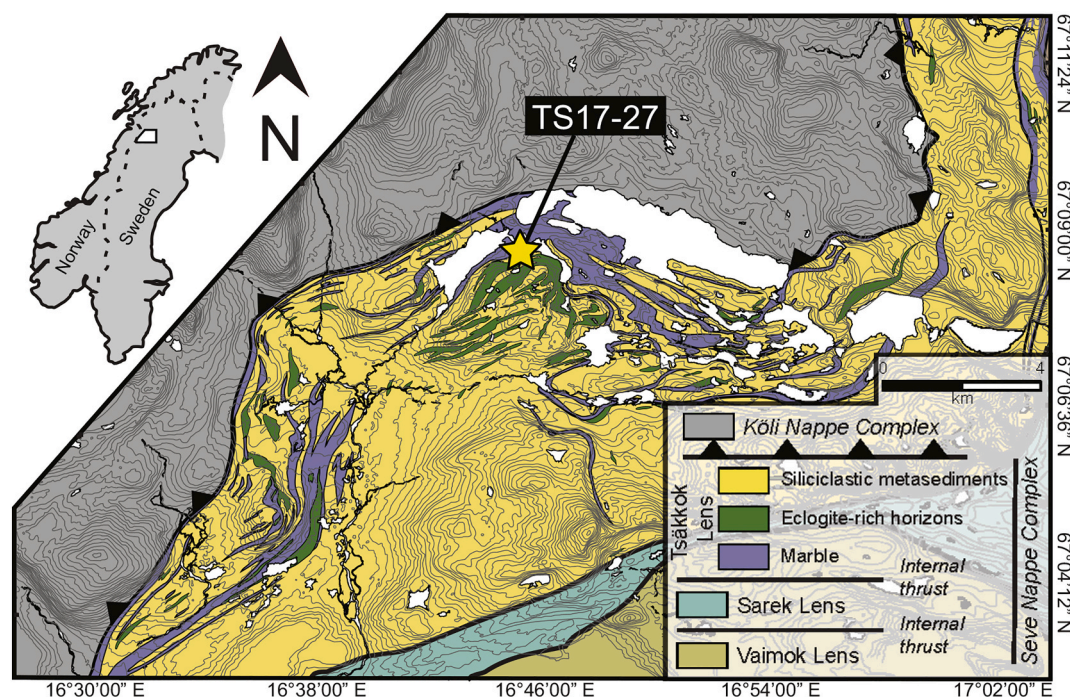


Fig. 1. Geological map of the Tsäkkok Lens and surrounding tectonic units in southern Norrbotten, Sweden, modified after Kullerud (1987) and Snijlsberg (1987). The location of the map is represented by the white polygon on the greyscale map of Scandinavia. The location of the studied white mica schist (sample TS17–27) is denoted by the yellow star. (For interpretation of the references to colour in this figure legend, the reader is referred to the web version of this article.)

situ on monazite in thin section during two analytical sessions at the Vegacenter, Swedish Museum of Natural History (Stockholm, Sweden) using an ESI NWR193 ArF excimer laser ablation system. Geochronological analyses were conducted during the first session and the trace element data were acquired during the second session. The grains were dated in numeric sequence (i.e., Mnz1 followed by Mnz2, etc.) rather than according to the monazite chemical zones. For both geochronological and trace element analyses, the laser was operated with a beam diameter of 6 μm at a frequency of 5 Hz and a fluence of 2 J/cm². Two pre-ablation bursts with a 9 μm beam diameter were conducted prior to each geochronological analysis to remove possible surface contamination. The locations of the ablations were chosen according to BSE images, EMP chemical maps and reflected light images of the monazite grains. After analysis, reflected light images of the monazite grains were re-taken to image the locations of the ablation pits.

For geochronological analyses, mass/charge values of 238, 235, 232, 208, 207, 206, 204, and 202 were measured using a Nu Plasma II multi-collector inductively-coupled plasma mass spectrometer (MC-ICP-MS) connected to the laser ablation system. Helium was used as the carrier gas with a flow rate of 0.35 L/min, which was then mixed with Ar gas at a flow rate of 0.91 L/min. A 20 s ablation time followed by a 15 s washout time with an integration time of 0.5 s were used for data collection. The data were collected with a 0.5 s integration time per data point. The data were processed using Iolite (Version 2.5, Paton et al., 2011) with the VizualAge data reduction scheme (Petrus and Kamber, 2012). The primary reference material used for data reduction was ‘monazite 44069’ (424.9 \pm 0.4 Ma; Aleinikoff et al., 2006). Managotry (555 \pm 2 Ma; Paquette and Tiepolo, 2007) and Skalna (c. 311 Ma; Szopa et al., 2017) monazite were used as secondary reference materials. All uncertainties are reported at the 2 σ level and include the propagated uncertainty from the primary reference material ‘monazite 44069’. All concordia plots and calculations were acquired using IsoplotR (v. 4.1) with the default decay constants and ²³⁸U/²³⁵U ratio (Vermeesch, 2018). The reported error correlations (ρ) for ²⁰⁷Pb/²³⁵U and ²⁰⁶Pb/²³⁸U were used for the Wetherill and Th-U-Pb concordia diagrams. Error correlations between other ratios were not used. When

necessary, the data were corrected for initial Pb using a (²⁰⁷Pb/²⁰⁶Pb)₀ value of 0.851 calculated using the Kramers and Tolstikhin (1997) model at 475 Ma.

For trace element (Sr, Y, REE) acquisition, an AttoM high-resolution inductively-coupled plasma mass spectrometer (HR-ICP-MS) was connected to the laser system. Helium was used as the carrier gas with a flow rate of 0.35 L/min, which was then mixed with Ar gas at a flow rate of 0.84 L/min. Data were collected during a 20 s ablation followed by a 20 s washout period. The data were processed using an in-house Excel spreadsheet. Results were normalized to the trace element composition of the primary reference material ‘monazite 44069’ (Aleinikoff et al., 2006; Holder et al., 2015). Managotry (Paquette and Tiepolo, 2007) and Moacry (Gonçalves et al., 2016) monazite were used as secondary reference materials for trace elements. The Y-in-Mnz thermometer of Pyle et al. (2001) was also applied to the monazite grains.

After geochronological and trace element analyses, all grains were imaged in reflected light to obtain the exact locations of the ablation pits for each monazite. The locations were overlaid on both EMP chemical maps and BSE images to identify analyses that ablated grain boundaries, fractures, inclusions, or that potentially mixed different chemical zones, all of which were rejected from further processing. The resulting data-sets were also scrutinized for erroneous data and were compared with the locations of ablation pits. The combination of ablation locations and identification of erroneous data were used as the basis to accept or reject each individual analysis.

4. Results

4.1. Petrographic description of the white mica schist

Structural investigations of the sampled outcrop indicated the preservation of prograde-to-peak foliation (S1) that was folded (F2) with weak axial-planar foliation development (S2) during exhumation of the Tsäkkok Lens (Barnes et al., 2020a). Transmitted light and electron microscopy conducted on the white mica schist (sample TS17–27) from the outcrop revealed a mineral assemblage of white mica, plagioclase,

quartz, a carbonate with an intermediate composition between siderite and magnesite, ankerite, chlorite, ilmenite, pyrite (or possibly marcasite), hydrous Fe-sulfate (possibly melanterite), apatite, monazite, rutile, xenotime, and zircon (Fig. 2). The sample is notably absent of garnet, or

of any pseudomorphs after garnet. White mica is the most abundant mineral in the rock and defines the evolution of the aforementioned structures (i.e., S1, F2, S2). Plagioclase, quartz, siderite-magnesite, ankerite, chlorite, Fe-sulphides, and ilmenite comprise the other

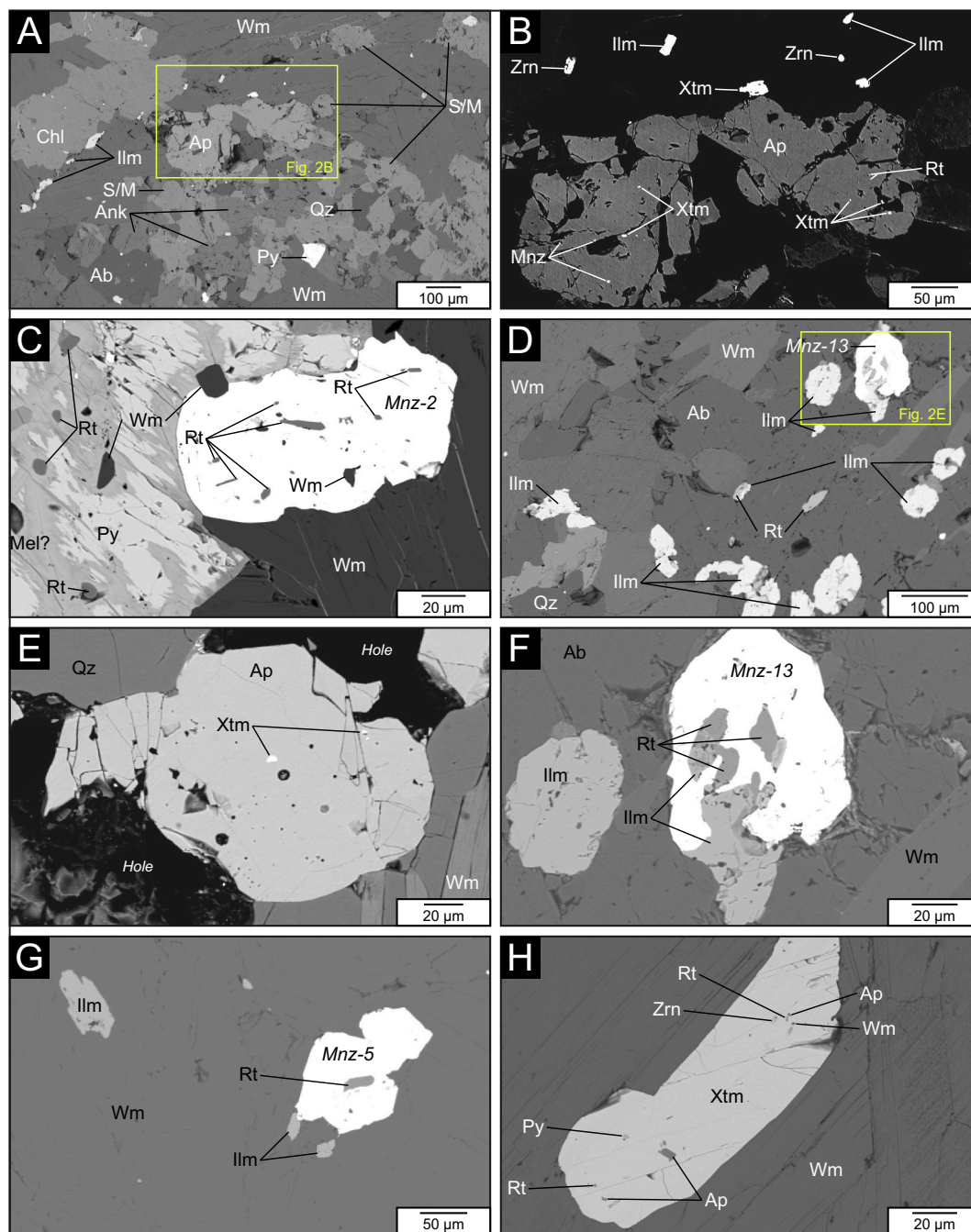


Fig. 2. Back-scattered electron images of minerals that comprise the studied white mica schist (sample TS17-27). A: General image showing the diverse mineralogy of the white mica schist. B: Enlarged, low-brightness/high-contrast image of the apatite grain in image A to show the spatial associations of apatite with monazite, rutile, and xenotime. Zircon and ilmenite are also present close to apatite, but they are in general more randomly distributed throughout the sample. C: Close-up image of a monazite grain (Mnz-2) exhibiting rutile inclusions within monazite that are located in the Mnz-I domain. The monazite grain is adjacent to a pyrite porphyroblast that is partially decomposed to melanterite(?) and also contains rutile inclusions. D: General image of an ilmenite-rich region in proximity to a monazite grain (Mnz-13). Two rare matrix rutile grains are present in the center of the image. The grain on the left is partially decomposed to ilmenite. E: Close-up of an equant, subhedral apatite grain. The grain shape indicates the section is cut perpendicular to the c-axis. Multiple pore-spaces are present within the apatite grain. Xenotime is also present in similarly shaped spaces. F: Enlarged image of the monazite grain (Mnz-13) in image D. The monazite grain has fully to partially included rutile grains that are incompletely decomposed to ilmenite where exposed to the matrix. G: A second example of a large rutile inclusion in monazite (Mnz-5 with ilmenite in the white mica-dominated matrix. H: The xenotime porphyroblast with inclusions of apatite, rutile, pyrite, zircon and white mica. Ab, albite; Ank, ankerite; Ap, apatite; Chl, chlorite; Ilm, ilmenite; Mel?, Melanterite(?); Mnz, monazite; Py, pyrite; Qz, quartz; Rt, rutile; S/M, siderite-magnesite; Wm, white mica; Xtm, xenotime, Zrn, zircon.

volumetrically significant minerals (Fig. 2A). Plagioclase forms porphyroblasts that host white mica inclusions that preserve S1. Siderite-magnesite and ankerite are found together throughout the sample (Fig. 2A) and are commonly accompanied by chlorite bundles that are concordant with the white mica. Iron sulphides are found as large porphyroblasts that contain inclusions of rutile, ilmenite, and white mica (Fig. 2C). The porphyroblasts are locally replaced by melanterite(?) along fractures and cleavage planes (Fig. 2C). Ilmenite grains are

randomly distributed and abundant throughout the matrix (Fig. 2D). The minor mineral constituents of the rock include apatite, monazite, rutile, xenotime, and zircon. Apatite is found in clusters and as individual grains (Fig. 2A, B, E). Monazite occurs as nearly equant to highly elongate grains (~20–200 μm long) that are evenly distributed throughout the rock without apparent textural relationships with other minerals (Fig. 2C, D, F, G). Smaller monazite grains ($\leq 5 \mu\text{m}$) located within apatite are also present (Fig. 2A, B). Rutile is predominantly

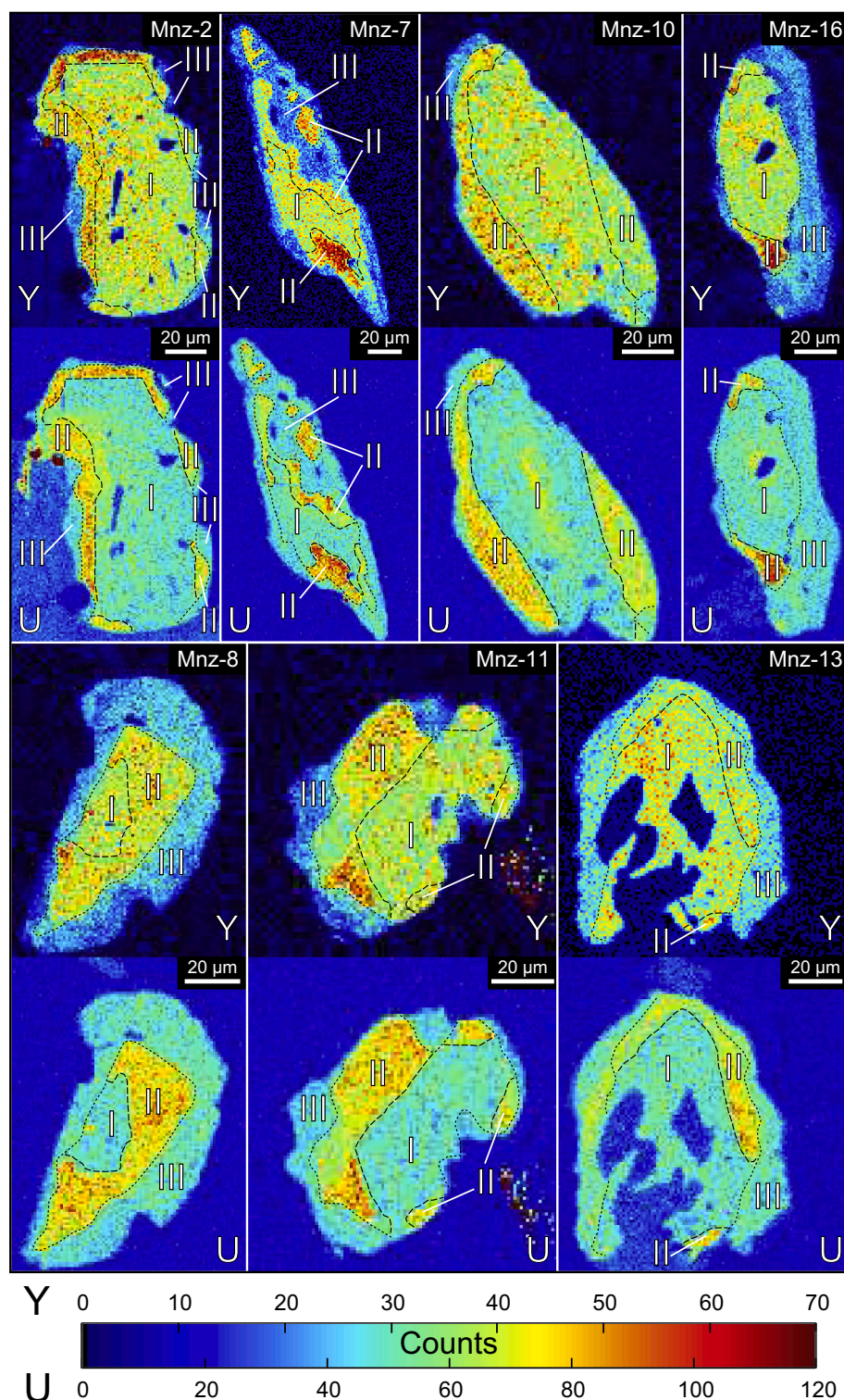


Fig. 3. Electron microprobe chemical maps of select monazite grains (top: Mnz-2, -7, -10, and -16; bottom: Mnz-8, -11, and -13). Two maps are presented for each grain (Y, upper panel; U, lower panel), collectively illustrating the textural relationships of the three monazite domains that are denoted by I (Mnz-I), II (Mnz-II), and III (Mnz-III). The dashed line represents the boundary between Mnz-I and Mnz-II, and the dotted line represents the approximate dissolution-precipitation front of Mnz-III. All maps were computed using XMapTools v. 2.6.4 (Lanari et al., 2014) referenced to the same scale bar for Y (top of the bar) and U (bottom of the bar). Monazite grains Mnz-2 and Mnz-13 are shown in Fig. 2C and E, respectively. The chemical maps here demonstrate that the rutile inclusions are present in the Mnz-I domain.

included in monazite, apatite, and pyrite (Fig. 2C, F, G), with only a few grains present in the mica-dominated matrix that are partially replaced by ilmenite (Fig. 2D). The replacement reaction also affected the rutile inclusions in the pyrite. One large porphyroblast of xenotime (~160 μm long) was found with inclusions of apatite, rutile, and zircon (Fig. 2H). Smaller xenotime grains ($\leq 5 \mu\text{m}$) are also located close to the apatite clusters (Fig. 2B), within apatite grains (Fig. 2B, E), and less commonly within monazite grains.

4.2. Monazite chemistry and Y-in-Mnz thermometry

Three generations of monazite are distinguished from the EMP chemical maps of all seventeen grains and are hereafter referred to as Mnz—I, Mnz—II and Mnz—III, and are best illustrated by maps of Y and U (Fig. 3). The maps show that Mnz—I defines the cores of the grains, Mnz—II is found as a mantle with a well-defined contact around the cores, and Mnz—III forms irregular rims with embayed, lobate boundaries with Mnz—II and sometimes Mnz—I. The trace element concentrations (oxide wt%) of SrO , Y_2O_3 , and REE_2O_3 were obtained from a total of 73 accepted trace element analyses that were accepted out of 78. The results are classified by monazite generation: Mnz—I (n: 35), Mnz—II (n: 18), and Mnz—III (n: 20). Additionally, the approximate amounts (oxide wt%) of ThO_2 and UO_2 were obtained from 85 (out of 125) LA-ICP-MS analyses that were purposed for geochronology for Mnz—I (n: 28), Mnz—II (n: 32), and Mnz—III (n: 25). The trace element data are summarized in Table 1. The complete dataset is available in Table S1 (for SrO , Y_2O_3 , and REE_2O_3) and Table S2 (for ThO_2 and UO_2).

Average values for Mnz—I are 0.31 wt% for UO_2 , 3.12 wt% for ThO_2 , 2.08 wt% for SrO , 4.03 wt% for Y_2O_3 , and 1.08 wt% for total HREE_2O_3 (Tb_2O_3 – Lu_2O_3). Compared to Mnz—I, the UO_2 values of Mnz—II are considerably higher (avg.: 1.19 wt%) and ThO_2 values are slightly elevated (avg.: 3.97 wt%); SrO is slightly lower (avg.: 1.60 wt%). The Y_2O_3 and HREE_2O_3 concentrations are slightly higher compared to Mnz—I (avgs.: 4.95 wt% and 1.33 wt%, respectively). The monazite maps also show that Ca is elevated in Mnz—II compared to Mnz—I (Fig. 3), but Ca content was not quantified. For Mnz—III, the UO_2 values (avg.: 0.24 wt%) are more similar to Mnz—I than Mnz—II. ThO_2 values (avg.: 3.85 wt%) overlap with both Mnz—I and Mnz—II. The SrO concentration (avg.: 1.40 wt%) is similar to Mnz—II. The Y_2O_3 concentrations (avg.: 2.31 wt%) and HREE_2O_3 (avg.: 0.76 wt%) are both significantly lower than for Mnz—I and Mnz—II.

Averages of all oxide values were obtained, and a temperature was calculated (Table 2) from each domain of each monazite grain where both geochronological (UO_2 , ThO_2 , and PbO) and trace element analyses (Y_2O_3 and REE_2O_3) were performed according to the calibration of Pyle et al. (2001). An average temperature ($\pm 2\sigma$ standard deviation) was then obtained from all domains of the same generation. The resulting temperatures are: $583 \pm 30^\circ\text{C}$ for Mnz—I, $624 \pm 67^\circ\text{C}$ for Mnz—II, and $473 \pm 80^\circ\text{C}$ for Mnz—III (Fig. 4; Table 2). It should be noted that the CaO content, which is required for the calibration of Pyle et al. (2001), was

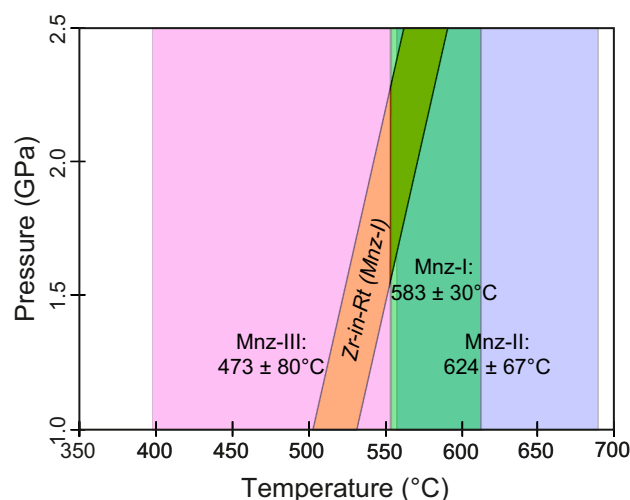


Fig. 4. Graphical summary of the results of Zr-in-Rt thermometry (orange polygon) for rutile inclusions in Mnz—I domains, and Y-in-Mnz thermometry for Mnz—I (green rectangle), Mnz—II (blue rectangle), and Mnz—III (purple rectangle). Note that the temperature range for Mnz—II almost completely overlaps with the temperature range of Mnz—I. (For interpretation of the references to colour in this figure legend, the reader is referred to the web version of this article.)

Table 2
Summary of Y-in-Mnz thermometry.

Monazite grain	Temperature ($^\circ\text{C}$) ^a		
	Mnz—I	Mnz—II	Mnz—III
Mnz1	559	–	–
Mnz2	565	589	–
Mnz4	571	–	462
Mnz5	–	–	500
Mnz7	584	–	–
Mnz8	581	631	526
Mnz9	600	635	427
Mnz10	584	624	–
Mnz11	583	600	–
Mnz13	601	600	–
Mnz14	601	689	–
Mnz16	585	–	451
Average	583	624	473
2 σ	30	67	79

^a Calculated with the calibration of Pyle et al. (2001)

not measured but a value of 0.5% was applied to Mnz—I and Mnz—II domains, and 1.0% provided for Mnz—II, considering the higher Ca content observed in the chemical maps (Fig. 3; Fig. S1). Although the exact values of CaO are not known, increasing CaO by an order of magnitude (i.e., from 0.5% to 5% for Mnz—I) only decreases the temperature by

Table 1
Summary of trace element data for the three monazite generations.

Rutile sample number	Nb_2O_5 (wt%)	TiO_2 (wt%)	FeO (wt%)	SiO_2 (wt%)	Al_2O_3 (wt%)	V_2O_3 (wt%)	Cr_2O_3 (wt%)	ZrO_2 (wt%)	Total (wt%)	Zr (ppm)	Average Zr (ppm)	$T(^{\circ}\text{C})^a$	
												1.0 GPa	2.5 GPa
Mnz2_Rt01	0.31	97.02	0.37	0.00	0.02	0.07	0.09	0.01	97.88	74.0	72.4	517 \pm 15	577 \pm 15
Mnz2_Rt03	0.44	95.50	0.55	0.01	0.03	0.02	0.03	0.01	96.58	59.2			
Mnz5_Rt01	0.41	97.99	0.40	0.00	0.03	0.02	0.05	0.01	98.91	81.4			
Mnz5_Rt02	0.42	98.19	0.38	0.00	0.02	0.02	0.04	0.01	99.08	51.8			
Mnz9_Rt01	0.27	97.27	0.34	0.00	0.01	0.00	0.08	0.01	97.97	59.2			
Mnz9_Rt02	0.30	97.35	0.30	0.01	0.01	0.02	0.08	0.01	98.07	88.8			
Mnz13_Rt01	0.51	97.62	0.54	0.01	0.02	0.05	0.04	0.01	98.80	88.8			
Mnz13_Rt02	0.49	97.44	0.43	0.00	0.02	0.00	0.05	0.01	98.44	59.2			
Mnz13_Rt04	0.78	96.68	0.62	0.00	0.02	0.00	0.05	0.01	98.16	88.8			

^a Calculated with the combined calibration of Kohn (2020) for the quartz stability field using the average Zr (ppm) value. Uncertainties are according to Kohn (2020).

~20 °C. Due to the estimated CaO values and the averaging of UO₂, ThO₂, and PbO, which are all approximate values, the resulting temperatures should be treated as 'semi-quantitative' approximations of the monazite crystallization temperatures but still demonstrate the relative thermal conditions between each monazite generation.

4.3. Zr-in-Rt thermometry

A total of twelve analyses were conducted on rutile included in the Mnz-I domains. Two analyses were rejected due to low weight oxide total (<96%). The concentration of Zr (ppm) was calculated for the remaining ten analyses. One more analysis was rejected that had a Zr value (29.6 ppm), which was lower than the detection limit of the analytical setup (~50 ppm Zr). The Zr concentrations of the nine accepted analyses range from 51.8 ppm to 88.9 ppm with an average of 72.4 ppm (Table 3). Temperature estimates were calculated using the pressure-dependent, combined dataset Zr-in-Rt thermometer calibration of Kohn (2020). Temperature was calculated from 1.0 to 2.5 GPa to assess the pressure dependence (Ferry and Watson, 2007). An uncertainty on the calibration of ±15 °C (2σ standard deviation) is applied to the resulting temperatures (Kohn, 2020), which range from 517 ± 15 °C at 1.0 GPa to 577 ± 15 °C at 2.5 GPa (Fig. 4).

4.4. Monazite geochronology

MC-ICP-MS analyses for geochronology were conducted across the primary reference monazite '44069' (n: 46) and secondary reference monazite 'Manangotry' (n: 8) and 'Skalna' (n: 11) that were interspersed between analyses of the seventeen Tsäkkok monazite grains (n: 125) over the analytical session. All the isotopic systems from the primary and secondary reference materials are within 2σ uncertainty of the ages of the reference materials, however, the ²⁰⁸Pb/²³²Th dates are slightly younger than the secondary reference ages whereas the ²⁰⁷Pb/²³⁵U and ²⁰⁶Pb/²³⁸U dates are older (Table S2). The analyses of all reference materials were plotted in Wetherill concordia space and ²⁰⁸Pb/²³²Th versus ²⁰⁶Pb/²³⁸U concordia space. Both methods provide concordia ages that are equivalent within uncertainty and overlap with the respective reference ages, except for the Wetherill concordia age for the Manangotry monazite that is older than the reference age (Fig. S2).

For the Tsäkkok monazite analyses, 85 analyses (of the 125) were deemed acceptable (Table S2; Fig. S1). The results of the geochronological analyses are divided based on the three monazite generations: Mnz-I (n: 28), Mnz-II (n: 32), and Mnz-III (n: 25). A c. 177 Myr span of dates is present for the collective decay systems (i.e., ²⁰⁶Pb/²³⁸U, ²⁰⁷Pb/²³⁵U, and ²⁰⁸Pb/²³²Th) for all three monazite generations. The ²⁰⁷Pb/²³⁵U dates are the oldest for all three generations, whereas the younger ²⁰⁶Pb/²³⁸U and ²⁰⁸Pb/²³²Th dates generally overlap (Table 4). Overall, Mnz-I provides the oldest dates, followed by Mnz-II, and the majority of the dates for Mnz-III are similar to the previous two with several, much younger dates (Table 4). The dates of Mnz-I and Mnz-II each define single populations at the 2σ uncertainty level. The dates of Mnz-III are less consistent but are predominantly due to eight analyses that are strongly dispersed towards younger dates. These eight analyses

were excluded from calculations of the weighted averages of the three isotopic systems and all the assessments of the data using the various concordia diagrams (Table 4).

Normal discordance of the ²⁰⁷Pb/²³⁵U versus ²⁰⁶Pb/²³⁸U dates is significant for all three monazite generations (Table 4) and shows a strong, negative correlation with Th/U ratios for Mnz-I and Mnz-II (Fig. 5A). In contrast, only slight normal discordance is present for the majority of the ²⁰⁶Pb/²³⁸U versus ²⁰⁸Pb/²³²Th dates (Table 4) and there is no observable trend with Th/U for Mnz-I and Mnz-II (Fig. 5A). Mnz-III does not follow any trends for discordance versus Th/U. The individual ²⁰⁶Pb/²³⁸U and ²⁰⁸Pb/²³²Th dates both decrease with increasing actinide content (Fig. 5B) and exhibit a slight increase of discordance proceeding towards higher actinide values.

To further scrutinize the datasets, each monazite generation was examined using 1) the Tera-Wasserburg concordia diagram, 2) the Wetherill concordia diagram, and 3) the Th-U-Pb concordia method of Vermeesch (2020), which utilizes all three isotopic systems but plots the results in ²⁰⁸Pb/²³²Th versus ²⁰⁶Pb/²³⁸U concordia space. In Tera-Wasserburg space, the uncorrected Mnz-I data form a discordant, well-defined linear array (Fig. 6A), uncorrected Mnz-II data plot as a discordant cluster with a linear aspect (Fig. 7A), and uncorrected Mnz-III results are also discordant with a weakly linear array with the eight analyses dispersed towards higher ²³⁸U/²⁰⁶Pb values (Fig. 8A). Model-1 regression lines were applied to the three datasets. Two regressions were conducted for each dataset, the first without any fixed intercepts (free-regression) and a second with an anchored upper-intercept at a (²⁰⁷Pb/²⁰⁶Pb)₀ value of 0.851, according to the model of Kramers and Tolstikhin (1997). The free-regression produced younger lower-intercept dates than the anchored-regression (Table 4), with the latter providing 479.3 ± 1.0 Ma for Mnz-I (MSWD: 1.3; Fig. 6A), 473.0 ± 1.4 Ma for Mnz-II (MSWD: 2.6; Fig. 7A), and 476.6 ± 2.3 Ma for Mnz-III (MSWD: 3.2; Fig. 8A). The (²⁰⁷Pb/²⁰⁶Pb)₀ values yielded by the free-regression are also all lower than that of the Kramers and Tolstikhin (1997) model.

Plotting uncorrected data in Wetherill concordia space also demonstrates the systematic normal discordance of these two systems for all generations (Figs. 6B, 7B, and 8B). Both Mnz-I and Mnz-II plot as normally discordant clusters with linear trends at a high angle to concordia, whereas Mnz-III is clustered with a younger dispersion of data that represent the same eight analyses that were excluded from the Tera-Wasserburg linear regression. The datasets were then corrected for initial Pb and replotted in Wetherill space. The resulting concordia dates are: 479.2 ± 0.8 Ma for Mnz-I (MSWD: 0.8; Fig. 6B and Table 4), 473.3 ± 1.0 Ma for Mnz-II (MSWD: 3.3; Fig. 7B and Table 4), and 476.5 ± 1.6 Ma for Mnz-III (MSWD: 2.0; Fig. 8B and Table 4).

The data for each generation were plotted in concordia space according to the method of Vermeesch (2020) that incorporates the three decay systems. The data for the three monazite generations plot as clusters on concordia in ²⁰⁸Pb/²³²Th versus ²⁰⁶Pb/²³⁸U space. The resulting concordia dates are: 484.7 ± 1.1 Ma for Mnz-I (MSWD: 1.4; Fig. 6C and Table 4), 474.7 ± 1.2 Ma for Mnz-II (MSWD: 1.9; Fig. 7C and Table 4), and 480.4 ± 2.1 Ma for Mnz-III (MSWD: 3.0; Fig. 8C and Table 4).

Table 3
Rutile chemistry and results of Zr-in-Rt thermometry.

Monazite generation	Number of analyses ^a	UO ₂ ^a (wt%)		ThO ₂ ^a (wt%)		Number of analyses ^b	SrO ^b (wt%)		Y ₂ O ₃ ^b (wt%)		ΣHREE ₂ O ₃ ^{b,c} (wt %)	
		Range	Avg.	Range	Avg.		Range	Avg.	Range	Avg.	Range	Avg.
Mnz-I	28	0.21–0.49	0.31	2.39–4.03	3.12	35	1.09–2.99	2.08	3.16–5.24	4.03	0.94–1.26	1.08
Mnz-II	32	0.64–2.09	1.19	3.23–5.11	3.97	18	0.83–2.16	1.60	4.03–6.11	4.95	1.14–1.53	1.33
Mnz-III	25	0.07–0.61	0.24	2.50–4.92	3.85	20	1.04–2.08	1.40	0.62–3.69	2.31	0.29–1.09	0.76

^a Values obtained from geochronological analysis.

^b Values obtained from trace element analysis

^c Sum of Tb₂O₃ to Lu₂O₃

Table 4

Summary of geochronological data for the three monazite generations.

		Mnz-I	Mnz-II	Mnz-III
Number of analyses		28	32	25
$^{207}\text{Pb}/^{235}\text{U}$ (Ma) dates	Range (Ma)	575.0 \pm 22.7 to 516.8 \pm 18.1	519.7 \pm 18.0 to 489.7 \pm 17.8	557.6 \pm 18.2 to 469.4 \pm 18.3
	Weighted average (Ma)	551.9 \pm 5.7 (MSWD: 2.6)	498.9 \pm 3.1 (MSWD: 0.6)	532.5 \pm 4.3 (MSWD: 0.8) ^a
$^{206}\text{Pb}/^{238}\text{U}$ (Ma) dates	Range (Ma)	493.1 \pm 5.1 to 479.3 \pm 5.3	483.9 \pm 5.7 to 466.0 \pm 5.0	489.3 \pm 5.1 to 419.0 \pm 4.9
	Weighted average (Ma)	485.3 \pm 1.2 (MSWD: 1.5)	475.0 \pm 1.4 (MSWD: 2.6)	481.2 \pm 2.3 (MSWD: 3.3) ^a
$^{208}\text{Pb}/^{232}\text{Th}$ (Ma) dates	Range (Ma)	494.8 \pm 18.0 to 467.3 \pm 18.0	493.8 \pm 18.0 to 458.0 \pm 17.7	499.7 \pm 18.0 to 398.1 \pm 17.1
	Weighted average (Ma)	477.9 \pm 3.3 (MSWD: 0.7)	469.7 \pm 3.1 (MSWD: 0.8)	469.2 \pm 4.9 (MSWD: 1.8) ^a
Discordance	$^{207}\text{Pb}/^{235}\text{U}$ vs. $^{206}\text{Pb}/^{238}\text{U}$ (%)	−9.2 to −19.1 (avg: −13.8)	−3.3 to −8.2 (avg: −5.0)	−6.6 to −18.1 (avg: −10.7)
	$^{206}\text{Pb}/^{238}\text{U}$ vs. $^{208}\text{Pb}/^{232}\text{Th}$ (%)	−3.1 to 1.6 (avg: −1.5)	−3.3 to 3.0 (avg: −1.2)	−6.4 to 2.1 (avg: −2.7)
Tera-Wasserburg concordia	Free-regression lower-intercept dates (Ma)	472.2 \pm 5.7 (MSWD: 1.6)	462.4 \pm 9.1 (MSWD: 3.1)	459.2 \pm 26.7 (MSWD: 3.4) ^a
	Free-regression ($^{207}\text{Pb}/^{206}\text{Pb}$) ₀	0.43 \pm 0.15	0.19 \pm 0.09	0.23 \pm 0.20
	Anchored-regression lower-intercept dates (Ma) ^b	479.3 \pm 1.0 (MSWD: 1.3)	473.0 \pm 1.4 (MSWD: 2.6)	476.6 \pm 2.3 (MSWD: 3.2) ^a
Wetherill concordia	Corrected concordia dates (Ma) ^b	479.2 \pm 0.8 (MSWD: 0.8)	473.3 \pm 1.0 (MSWD: 3.3)	476.5 \pm 1.6 (MSWD: 2.0) ^a
Th-U-Pb concordia	Uncorrected concordia dates (Ma)	484.7 \pm 1.1 (MSWD: 1.4)	474.7 \pm 1.2 (MSWD: 1.9)	480.4 \pm 2.1 (MSWD: 3.0) ^a

^a Results produced by excluding 8 analyses affected by Pb-loss.^b Initial Pb composition anchored/corrected using a ($^{207}\text{Pb}/^{206}\text{Pb}$)₀ value of 0.851 calculated from the model of Kramers and Tolstikhin (1997).

5. Discussion

5.1. Evolution of monazite during retrogression from eclogite- to greenschist-facies

Eclogites in the Tsäkkok Lens record a HP metamorphic history, reaching 2.4–2.6 GPa and 560–680 °C (Bukała et al., 2020; Fassmer et al., 2021). Remnants of a HP mineral assemblage in the investigated white mica schist is represented by siderite-magnesite and the presence of rutile inclusions in Mnz-I domains, apatite, and pyrite. The association of siderite-magnesite with ankerite strongly resembles the carbonate phase relationships described for Fe-rich eclogites in Western Tianshan that record peak P-T conditions of 2.5 GPa and 550 °C (Tao et al., 2014). In such rocks, siderite-magnesite is the stable phase at peak conditions with ankerite (dolomite) stable at lower pressures. Rutile is typically the Ti-bearing phase at HP (Zack and Kooijman, 2017). The combined results of Zr-in-Rt and Y-in-Mnz thermometry provides P-T conditions of 1.5–2.5 GPa and 550–590 °C, although these estimates are

only approximate provided the Y-in-Mnz temperature should be treated as a semi-quantitative estimate. Furthermore, the validity of Y-in-Mnz thermometry requires xenotime to be present in the rock to buffer Y (Pyle et al., 2001). Xenotime has a large stability field in metapelitic rocks but its presence is typically controlled by garnet as xenotime is typically consumed near the garnet-in reaction during prograde metamorphism (Bea and Montero, 1999; Pyle and Spear, 2003a; Spear and Pyle, 2010). However, there is no indication that garnet existed in the white mica schist, so it is plausible that xenotime was present throughout the metamorphic history of the schist. The P-T estimates for the first generation of monazite are similar to previous estimate of eclogite-facies metamorphism for the Tsäkkok Lens (Bukała et al., 2020; Fassmer et al., 2021). As a result, Mnz-I likely crystallized during prograde to (near-)peak metamorphism in the lens (Fig. 9). This is also reflected by the high SrO content of Mnz-I (Finger and Krenn, 2007), which is highest of all generations (Table 1).

The textural relationships of Mnz-I and Mnz-II domains, revealed by chemical maps, indicate that Mnz-II represents overgrowths on the Mnz-

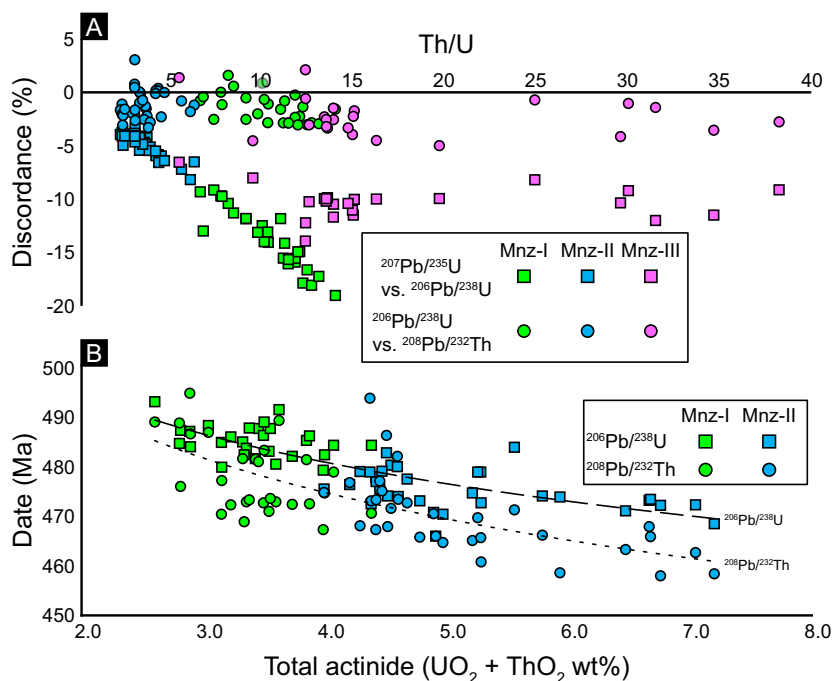
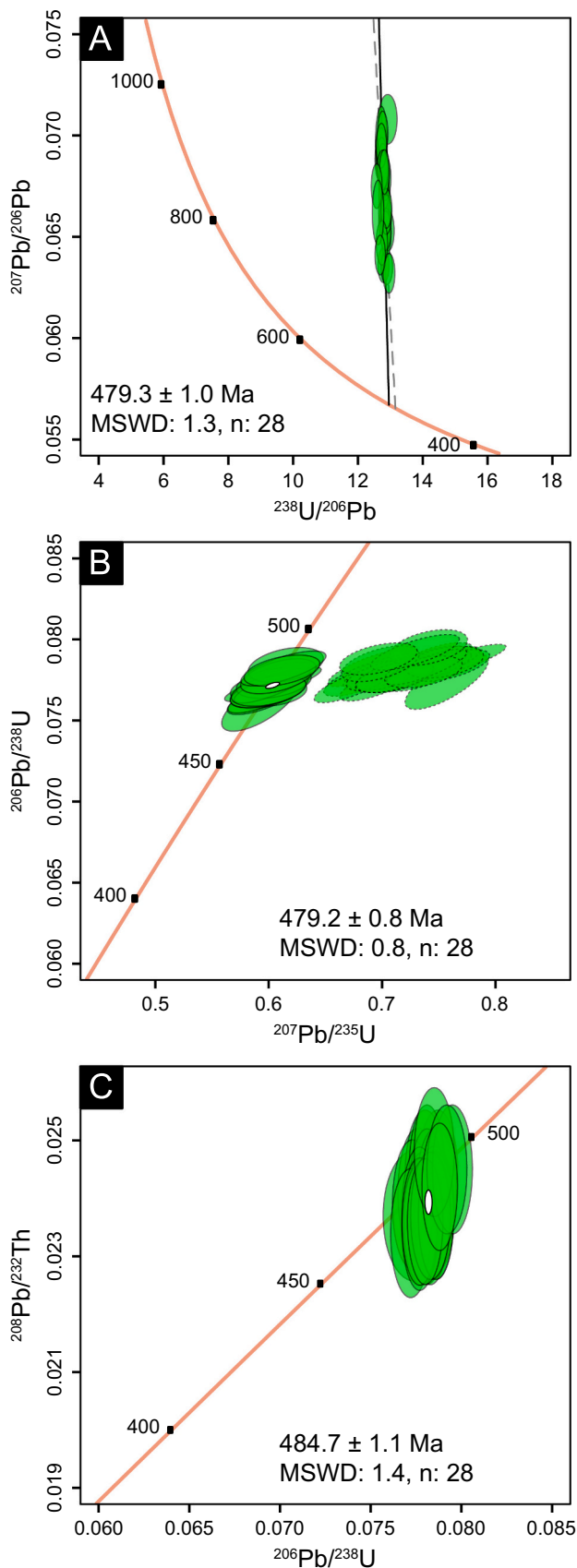


Fig. 5. Graphical plots illustrating the trends between dates and actinides content. A: The trends between discordance (i.e., $^{207}\text{Pb}/^{235}\text{U}$ versus $^{206}\text{Pb}/^{238}\text{U}$ and $^{206}\text{Pb}/^{238}\text{U}$ versus $^{208}\text{Pb}/^{232}\text{Th}$) and the Th/U ratio for all three monazite generations. All data from Mnz-III is included in the plot except for two points with the highest Th/U ratios. These points were excluded to provide better resolution of plot but follow the same pattern as the rest of the Mnz-III data points. Negative discordance values designate normal discordance and positive discordance values designate positive discordance. B: Individual $^{206}\text{Pb}/^{238}\text{U}$ and $^{208}\text{Pb}/^{232}\text{Th}$ dates as a function of actinide content (UO₂ + ThO₂) for both Mnz-I and Mnz-II. The trend-lines represent the trends of the collective dates (dashed: $^{206}\text{Pb}/^{238}\text{U}$, dotted: $^{208}\text{Pb}/^{232}\text{Th}$) for both monazite generations. Mnz-III was excluded to provide better resolution of Mnz-I and Mnz-II datasets but does not show a strong correlation with increasing actinide content.

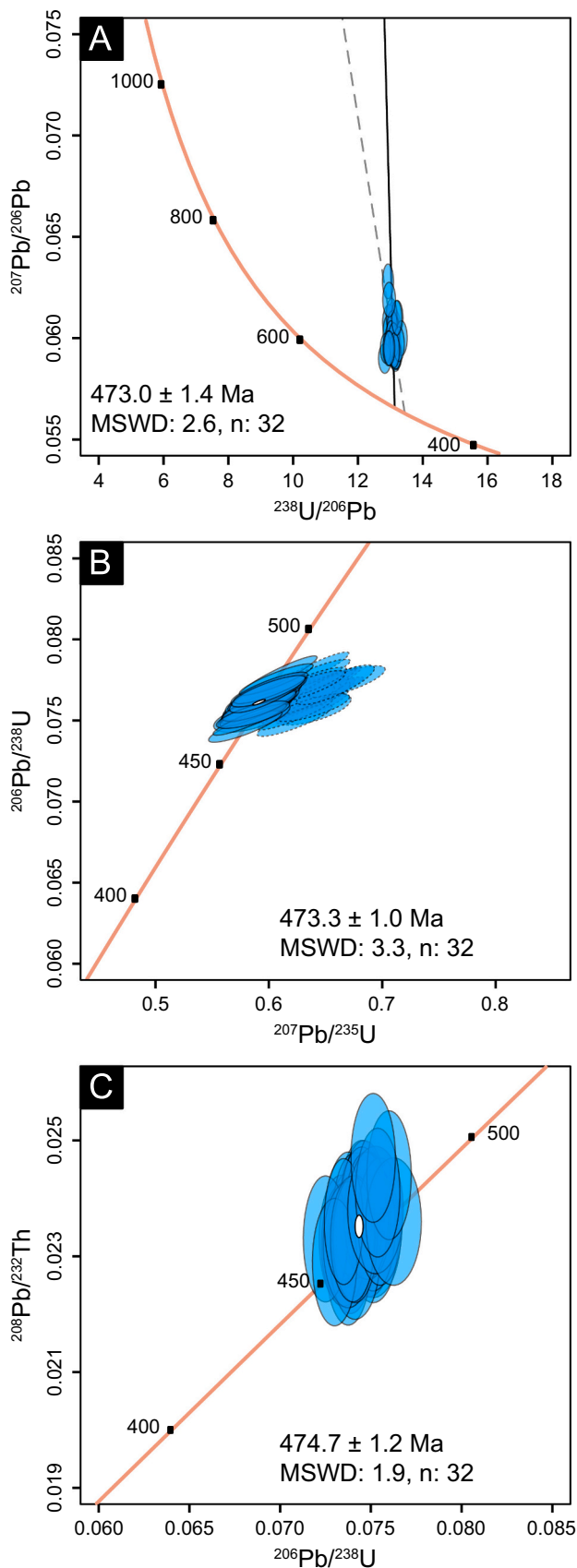


(caption on next column)

Fig. 6. Examination of isotopic data for Mnz-I in concordia space using IsoplotR (Vermeesch, 2018). A: Uncorrected data plotted in Tera-Wasserburg concordia space. Model-I linear regression (dashed line) was conducted in IsoplotR to obtain the upper- and lower-intercepts. The free-regression is represented by the dashed grey line and the anchored-regression is shown by the solid black line. The reported lower-intercept is from the anchored-regression. B: Uncorrected data (dashed ellipses) and corrected data (solid ellipses) plotted in Wetherill concordia space. The data were corrected using the terrestrial Pb evolution model of Kramers and Tolstikhin (1997). C: Uncorrected data with the analytical uncertainties propagated from the primary reference material and plotted according to Vermeesch (2020) in $^{206}\text{Pb}/^{238}\text{U}$ vs. $^{206}\text{Pb}/^{232}\text{Th}$ concordia space.

I cores (Fig. 3). A lower pressure origin of Mnz-II, compared to Mnz-I, is suggested by the decrease of Sr content and the increase of U (Table 1). The plagioclase within the sample has an almost pure albite composition, so the presence of plagioclase cannot explain the decrease of SrO from Mnz-I to Mnz-II as it would require a significant anorthite component to sequester Sr in place of Ca, as has been suggested to control Sr in metamorphic monazite (e.g., Krenn and Finger, 2004; Holder et al., 2015). However, the compatibility of Sr and Ca suggests that the decrease is due to sequestration by ankerite, which is the lower pressure carbonate phase in the rock (Tao et al., 2014). The increase of U requires contemporaneous metamorphic reaction(s) providing U. Dissolution of pre-existing apatite may help to explain the growth of new monazite (Finger and Krenn, 2007) with elevated U and Ca content observed for Mnz-II, with respect to Mnz-I (Fig. 2A, B). Furthermore, abundant pores (voids) and xenotime inclusions observed in apatite cut perpendicular to its c-axis (Fig. 2E) demonstrate dissolution-reprecipitation of apatite to produce the other phosphate minerals (Harlov and Förster, 2003; Harlov et al., 2005; Jonsson et al., 2016). The increase of U could also be a result of the breakdown of rutile to ilmenite, a typical decompression reaction (Korneliussen et al., 2000; Zack and Kooijman, 2017; Su et al., 2018) that was a volumetrically significant effect throughout the rock. The Fe needed for such reaction could have been supplied by decompression breakdown of siderite-magnesite to ankerite (Tao et al., 2014), or the change from ankerite to a more dolomitic composition. As a result, the geochronological and geochemical traits of Mnz-II strongly suggest growth in lower pressure conditions than Mnz-I (Fig. 9). However, the Y-in-Mnz thermometry suggests higher temperatures compared to Mnz-I (Fig. 4; Table 2). The higher temperatures may be a result of CaO content possibly greater than 1% or the high ThO₂ content of Mnz-II (Table 1), which increases Y₂O₃, thus increasing the calculated crystallization temperature (Seydoux-Guillaume et al., 2002). The overlap between Mnz-I and Mnz-II, however, may suggest that the Tsäkkok Lens experienced near-isothermal decompression through pressures of ~0.6–1.0 GPa (Fig. 9; Kullerud, 1987; Snijlsberg, 1987), similar to the underlying Vaimok Lens (Bukała et al., 2018).

The domains of Mnz-III typically exhibit highly irregular grain boundaries against Mnz-I and Mnz-II domains, commonly with embayed contacts, and possible relics of previous monazite encapsulated in the Mnz-III domains (Fig. 3; Fig. S1). The embayed, irregular boundaries suggest dissolution-reprecipitation of pre-existing monazite (Rasmussen and Muhling, 2007, 2009; Williams et al., 2011; Seydoux-Guillaume et al., 2012; Wawrzynitz et al., 2012; Grand'Homme et al., 2016; Seydoux-Guillaume et al., 2018b; Barnes et al., 2020b), which is also evinced by the cluster of dates similar to those of Mnz-I and Mnz-II, with eight dates that are significantly younger (Table S2). In such case, the similar Th content of Mnz-III to Mnz-I and Mnz-II, together with dispersion of dates, would reflect Th inheritance with partial resetting of the isotope signature of the pre-existing monazite volumes. However, the U content of Mnz-III is generally the lowest of all monazite generations and the loss of U coupled with only partial Pb-loss would result in some reverse discordance that is not observed for Mnz-III analyses. It is also possible that Mnz-III represents new monazite growth with high Th/



(caption on next column)

Fig. 7. Examination of isotopic data for Mnz-II in concordia space using IsoplotR (Vermeesch, 2018). A: Uncorrected data plotted in Tera-Wasserburg concordia space. Model-I linear regression (dashed line) was conducted in IsoplotR to obtain the upper- and lower-intercepts. The free-regression is represented by the dashed grey line and the anchored-regression is shown by the solid black line. The reported lower-intercept is from the anchored-regression. B: Uncorrected data (dashed ellipses) and corrected data (solid ellipses) plotted in Wetherill concordia space. The data were corrected using the terrestrial Pb evolution model of Kramers and Tolstikhin (1997). C: Uncorrected data with the analytical uncertainties propagated from the primary reference material and plotted according to Vermeesch (2020) in $^{206}\text{Pb}/^{238}\text{U}$ vs. $^{206}\text{Pb}/^{232}\text{Th}$ concordia space.

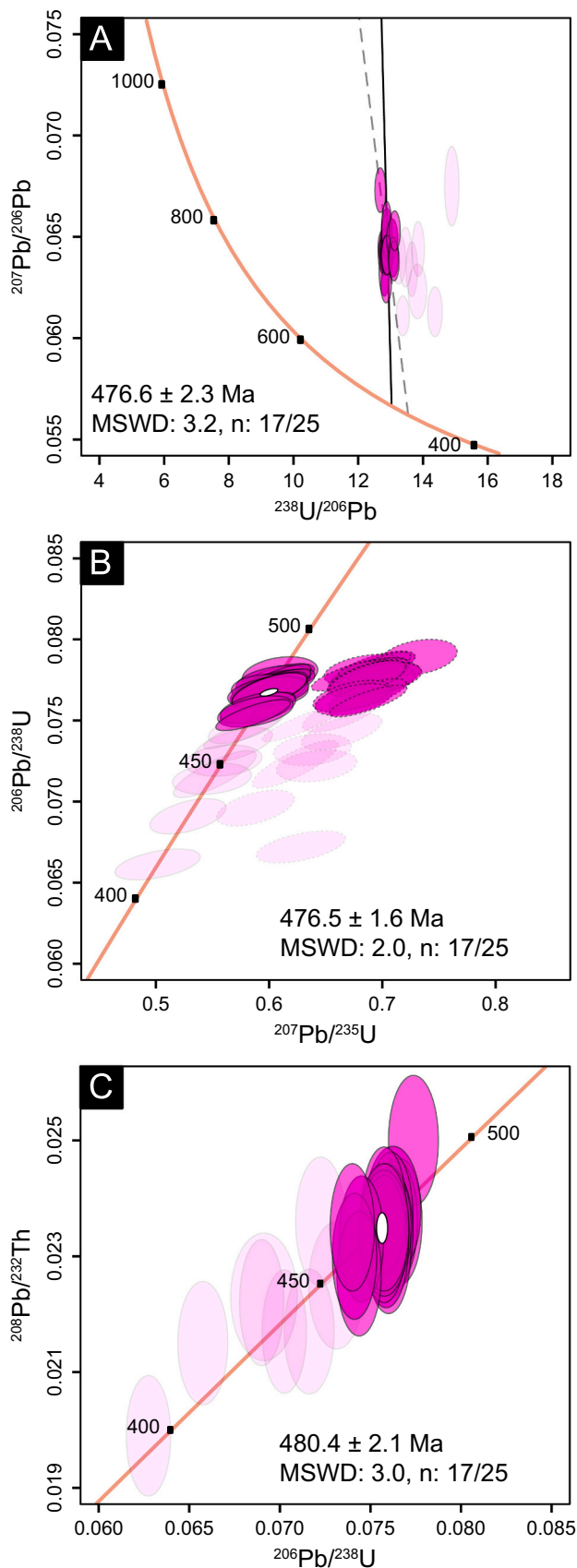
U that was subsequently nearly overprinted by dissolution-precipitation that also penetrated Mnz-I and Mnz-II domains. The lower Y and HREE content of Mnz-III, together with the presence of xenotime inclusions in the Mnz-III domains, provides Y-in-Mnz temperatures indicative of lower-amphibolite to upper-greenschist facies conditions (Fig. 4).

5.2. Comparison of the dataset assessment in Tera-Wasserburg, Wetherill, and $^{206}\text{Pb}/^{238}\text{U}$ vs. $^{206}\text{Pb}/^{232}\text{Th}$ concordia space

The discordance of the $^{207}\text{Pb}/^{235}\text{U}$ versus $^{206}\text{Pb}/^{238}\text{U}$ systems is evident in both Tera-Wasserburg and Wetherill concordia spaces for all three monazite domains. There are several possible causes for the discordance: 1) mixing of domains; 2) intermediate daughter product disequilibrium; 3) presence of initial Pb; 4) analytical artefacts; and 5) mobilization of Pb. Considering the screening process that was applied for accepting analyses, domain mixing or contamination (i.e., from fracture infill or inclusions) is not a likely explanation. Since the monazite possess a high Th content, it is possible that incorporation of ^{230}Th may have contributed to disequilibrium of $^{206}\text{Pb}/^{238}\text{U}$, but the effects should not be significant in Paleozoic monazite (Schärer, 1984; Parrish, 1990), and such disequilibrium is not supported by decreasing $^{206}\text{Pb}/^{238}\text{U}$ dates with increasing ThO_2 content (Fig. 5B). Therefore, the first two possibilities of discordance are not regarded to be significant for the Tsäkkok Lens monazite.

The linear array of the discordant data for all generations in Tera-Wasserburg and Wetherill space, being at a high angle to concordia in the latter, are indicative of an initial Pb component (Petrus and Kamber, 2012; Schoene, 2014). Although initial Pb contamination results in erroneously older dates, the magnitude of the effect is controlled by the actinide content of the monazite such that higher actinide content equates to greater radiogenic Pb that “dilutes” the initial Pb. The increase of $^{207}\text{Pb}/^{235}\text{U}$ versus $^{206}\text{Pb}/^{238}\text{U}$ discordance with increasing Th/U is a consequence of initial Pb contamination (Fig. 5A). The decrease of Th/U is primarily controlled by an increase of UO_2 (Table 1). Therefore, the pattern reflects the high sensitivity of the two U–Pb systems with initial Pb contamination, which is more significant in monazite with lower UO_2 . In contrast, $^{206}\text{Pb}/^{238}\text{U}$ versus $^{206}\text{Pb}/^{232}\text{Th}$ discordance does not change significantly with variations of Th/U due to the insensitivity of $^{206}\text{Pb}/^{232}\text{Th}$ in comparison to $^{207}\text{Pb}/^{235}\text{U}$. Mnz-III provides the highest Th/U values yet does not show the same pattern of discordance for $^{207}\text{Pb}/^{235}\text{U}$ versus $^{206}\text{Pb}/^{238}\text{U}$. The lack of trend is likely the result of partial Pb-loss and disturbance of the original initial Pb trend if it indeed formed from Mnz-I and Mnz-II. Therefore, the next parts of the discussion will pertain to Mnz-I and Mnz-II generations as the initial Pb trend is preserved.

Although the $^{206}\text{Pb}/^{238}\text{U}$ versus $^{206}\text{Pb}/^{232}\text{Th}$ dates fall near concordia, they are predominantly normally discordant as $^{206}\text{Pb}/^{232}\text{Th}$ dates are consistently younger than $^{206}\text{Pb}/^{238}\text{U}$ dates for the same analyses (Fig. 5A; Table 4). A trend between increasing actinide content with decreasing dates and slightly increasing discordance is also noticed for these two isotopic systems (Fig. 5B). The increase in discordance is opposite of the initial Pb contamination trend and suggests that there is



(caption on next column)

Fig. 8. Examination of isotopic data for Mnz-III in concordia space using IsoplotR (Vermeesch, 2018). A: Uncorrected data plotted in Tera-Wasserburg concordia space. Model-I linear regression (dashed line) was conducted in IsoplotR to obtain the upper- and lower-intercepts. The free-regression is represented by the dashed grey line and the anchored-regression is shown by the solid black line. The reported lower-intercept is from the anchored-regression. B: Uncorrected data (dashed ellipses) and corrected data (solid ellipses) plotted in Wetherill concordia space. The data were corrected using the terrestrial Pb evolution model of Kramers and Tolstikhin (1997). C: Uncorrected data with the analytical uncertainties propagated from the primary reference material and plotted according to Vermeesch (2020) in $^{206}\text{Pb}/^{238}\text{U}$ vs. $^{206}\text{Pb}/^{232}\text{Th}$ concordia space. For all plots, the pale ellipses represent the eight analyses that were excluded from calculation of the concordia dates in the respective plots.

an extra element of discordance affecting Mnz-I and Mnz-II. The secondary reference monazite analyses suggest some discordance resulting from an analytical artefact. For both secondary reference monazites, $^{208}\text{Pb}/^{232}\text{Th}$ dates are consistently younger than the $^{207}\text{Pb}/^{235}\text{U}$ and $^{206}\text{Pb}/^{238}\text{U}$ dates (Table S2). The discrepancy of the systems can also be reflected in the Tsäkkok monazite analyses. However, the dates of the secondary reference monazites do not explain the slight correlation between increasing actinide content and decreasing dates for Mnz-I and Mnz-II. Furthermore, the dates of all isotopic systems generally overlap with the secondary reference ages within 2σ uncertainty and the concordia ages calculated in Wetherill and Th-U-Pb concordia space are equal for the respective secondary reference monazite (Fig. S2). A similar pattern is observed for Mnz-II as the results from all concordia methods overlap within uncertainty, yet Mnz-I provides significantly younger dates from Wetherill (and Tera-Wasserburg) concordia diagrams compared to Th-U-Pb concordia (Fig. 6; Table 4). The inconsistency of the Mnz-I concordia diagrams compared to the consistency of Mnz-II and the secondary reference concordia diagrams cannot be explained as an analytical artefact.

Pb-loss is not expected from Mnz-I and Mnz-II domains as they provide no obvious evidence for dissolution-reprecipitation and the Tsäkkok Lens did not approach the conditions required for volume diffusion of Pb in monazite ($\sim 800^\circ\text{C}$; e.g., Kamber and Moorbath, 1998; Cherniak et al., 2004) and natural monazite does not become metamict (Meldrum et al., 1998; Seydoux-Guillaume et al., 2003; Ruschel et al., 2012; Nasdala et al., 2018; Seydoux-Guillaume et al., 2018a; Nasdala et al., 2020). It is also unlikely that the additional discordance of Mnz-I and Mnz-II is related to ablation of Mnz-III at depth as there is no obvious mixing between Mnz-I/Mnz-II with Mnz-III nor do the data trend towards Mnz-III datapoints in discordance versus Th/U space (Fig. 5A). Instead, the decreasing $^{208}\text{Pb}/^{232}\text{Th}$ and $^{206}\text{Pb}/^{238}\text{U}$ dates with increasing actinide content with a slight increase in discordance (Fig. 5B) suggests that Pb may be preferentially mobilized (i.e., redistributed within the grain) from domains with higher actinide content. Nanoclusters of Pb in monazite attest to Pb-mobilization, which is not thought to be related to volume diffusion (Fougereuse et al., 2018). The mobilization of Pb may be related to steady-state levels of radiation damage in natural monazite (Seydoux-Guillaume et al., 2003; Nasdala et al., 2020; Budzyń et al., 2021), alpha-recoil during decay events (Romer, 2003), and the incorporation of Th and U into the monazite structure, which creates lattice distortions (Raison et al., 2012; Ruschel et al., 2012) that are similar to those created by radiation damage (Raison et al., 2008). The lattice distortions could focus recrystallization and movement of dislocations in monazite in response to deformation (Erickson et al., 2015; Fougereuse et al., 2021), as has been observed for impurities in other mineral phases that has been shown to foster trace element mobility (e.g., Dubosq et al., 2021). Higher-resolution imaging and analyses of the Pb distribution in the Tsäkkok monazite would be necessary in future research to elucidate the nature of Pb mobilization. Nevertheless, the previous studies demonstrate that Pb-mobilization in monazite below the Pb closure temperature is a critical issue that needs to be considered for monazite geochronology and can provide a possible

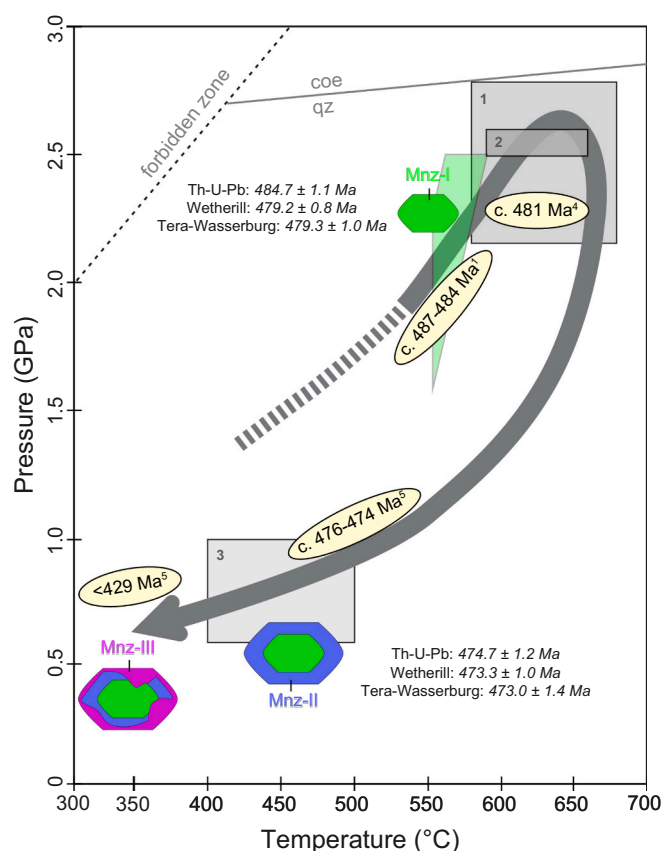


Fig. 9. Graphical P-T-t summary with the evolution of the monazite in the white mica schist of the Tsäkkok Lens. The P-T pathway is derived from P-T conditions obtained by previous studies, denoted by the grey boxes. The green polygon represents the P-T space defined by the intersection of Y-in-Mnz and Zr-in-Rt thermometry for crystallization of Mnz-I. The reported lower-intercept is from the anchored-regression. The timing of different P-T conditions from independent studies are indicated by the dates in the ellipses. The growth stages and relative timing of dissolution-reprecipitation of the monazite are represented along the P-T pathway. The results obtained from various methods for Mnz-I and Mnz-II are presented. The results of Mnz-III are not presented as the timing of formation is uncertain. ¹Fassmer et al. (2021); ²Bukala et al. (2020); ³Snijlsberg (1987); ⁴Root and Corfu (2012); ⁵Barnes et al. (2020). (For interpretation of the references to colour in this figure legend, the reader is referred to the web version of this article.)

explanation for the decrease of dates with increasing actinide content.

It is evident that the $^{208}\text{Pb}/^{232}\text{Th}$ and $^{206}\text{Pb}/^{238}\text{U}$ systems are not significantly affected by initial Pb contamination and provide the most robust method of assessing the crystallization age of the monazite. Due to the sensitive discordance of $^{207}\text{Pb}/^{235}\text{U}$ versus $^{206}\text{Pb}/^{238}\text{U}$ (predominantly controlled by the former), the subtle Pb-mobilization is masked and lower-intercept/Pb-corrected concordia dates obtained from the Tera-Wasserburg Wetherill concordia diagrams is indicative of initial Pb overcorrection. The behaviour of the overcorrection can be observed when comparing the free-regression with the anchored-regression in Tera-Wasserburg concordia space (Fig. 6A), as the former produced a younger lower-intercept date and a lower $(^{207}\text{Pb}/^{206}\text{Pb})_0$ value compared to the model of Kramers and Tolstikhin (1997). However, even the anchored-regression and initial Pb correction in Wetherill concordia space still reveal a significant overcorrection. Interestingly, although Mnz-II also provides evidence for Pb-mobilization, the overcorrection is not as pronounced as for Mnz-I and the results of all concordia methods are the same within uncertainty (Table 4). The dilution of initial Pb due to the higher UO_2 content of Mnz-II, resulting in lower discordance compared to Mnz-I, prevents the significant

overcorrection as there is less potential for an erroneous projection to concordia by the regression/correction. Thus, although both Mnz-I and Mnz-II are contaminated by initial Pb and show evidence of Pb-mobilization, the UO_2 content and relative dilution of initial Pb ultimately controls the magnitude of the overcorrection. Utilizing the Th-U-Pb concordia method of Vermeesch (2020), which incorporates all three isotopic systems, demonstrates that the inclusion of the $^{208}\text{Pb}/^{232}\text{Th}$ system is critical for extracting the correct crystallization ages for monazite affected by initial Pb, especially when UO_2 content is low. The overlap of age within uncertainty of all analyses in $^{206}\text{Pb}/^{238}\text{U}$ versus $^{208}\text{Pb}/^{232}\text{Th}$ concordia space indicates that discordance due to Pb-mobilization is less than the 2σ uncertainty of the individual analyses and is propagated into the uncertainty of the concordia age as it accounts for the dispersion of the data. Nevertheless, improving the precision of the analyses would help to identify and treat the slight discordance produced by Pb-mobilization.

The Th-U-Pb concordia dates of 484.7 ± 1.1 Ma for Mnz-I and 474.7 ± 1.2 Ma for Mnz-II are regarded as the crystallization ages of the monazite. The ages directly overlap with the timing of prograde metamorphism (487.7 ± 4.6 Ma to 484.6 ± 4.5 Ma; Fassmer et al., 2021; Fig. 9) leading to eclogite-facies metamorphism (481.9 ± 1.1 Ma; Root and Corfu, 2012), followed by post-decompression cooling of the lens (477.2 ± 4.1 Ma to 475.3 ± 3.5 Ma; Barnes et al., 2020a; Fig. 9). These results fit the interpretation of high-pressure monazite crystallization (Mnz-I) followed by growth of monazite following decompression (Mnz-II), as discussed in the previous section (Fig. 9). For Mnz-III, the timing of formation is less certain. The intermediate results between Mnz-I and Mnz-II may reflect a mixing of the older domains. The dispersed analyses that show partial Pb-loss also indicate that dissolution-reprecipitation may have occurred during Scandian deformation of the Tsäkkok Lens ($\leq 429.9 \pm 9.0$ Ma; Barnes et al., 2020a). This timing fits with the interpretation that Mnz-III formed in lower amphibolite- to upper greenschist-facies conditions.

6. Conclusions

Three generations of monazite are recognized from a single white mica schist from the Tsäkkok Lens that represent the evolution of the Lens from eclogite- to amphibolite/greenschist-facies conditions. Evaluation of the dataset for each generation in Tera-Wasserburg and Wetherill concordia space indicate an initial Pb component in the monazite and significant partial Pb-loss of the third monazite generation. The magnitude of discordance produced by initial Pb is controlled by the UO_2 content of the monazite. The UO_2 content equates to greater radiogenic Pb, which dampens the effect of initial Pb. Additional discordance is suggested to result from Pb-mobilization within Mnz-I and Mnz-II domains. The sensitivity of the $^{207}\text{Pb}/^{235}\text{U}$ and $^{206}\text{Pb}/^{238}\text{U}$ isotopic systems to the effects of initial Pb masks additional, secondary sources of discordance, leading to overcorrection of the datasets that is more pronounced in monazite with low UO_2 . The relative insensitivity of $^{208}\text{Pb}/^{232}\text{Th}$ allows the Th-U-Pb concordia method to account for both initial Pb and Pb-mobilization effects and provides reliable crystallization ages of Mnz-I and Mnz-II generations. The final results indicate that Mnz-I formed at 484.7 ± 1.1 Ma, and Mnz-II grew at 474.7 ± 1.2 Ma. The timing of the Mnz-III formation is not well-resolved as it likely formed via result of dissolution-reprecipitation of the pre-existing monazite and the isotopic systems are significantly disturbed.

Supplementary data to this article can be found online at <https://doi.org/10.1016/j.chemgeo.2021.120450>.

Declaration of Competing Interest

The authors declare that they have no known competing financial interests or personal relationships that could have appeared to influence the work reported in this paper.

Acknowledgements

M. Bukala and I. Klonowska are thanked for assistance during fieldwork in the Tsäkkok Lens. Editor B. Kamber, reviewer D. Davis, and an anonymous reviewer are sincerely thanked for their comments and constructive criticisms that have significantly improved the quality and scope of the manuscript. Funding for this research was provided by the National Science Centre of Poland (CALSUB project no. 2014/14/E/ST10/00321 to J. Majka). Other financial support for the completion of the research was given by the Polish National Agency for Academic Exchange (Iwanowska Programme scholarship no. PPN/IWA/2018/1/00030/U/00001 to C. Barnes). The Swedish Research Council is thanked for financial support to the Vegacenter national laboratory (Dnr. 2017-00671). This is Vegacenter publication number #044.

References

- Aleinkoff, J.N., Schenck, W.S., Plank, M.O., Srogi, L., Fanning, C.M., Kamo, S.L., Bosbyshell, H., 2006. Deciphering igneous and metamorphic events in high-grade rocks of the Wilmington complex, Delaware: Morphology, cathodoluminescence and backscattered electron zoning, and SHRIMP U-Pb geochronology of zircon and monazite. *Bull. Geol. Soc. Am.* 118, 39–64. <https://doi.org/10.1130/B25659.1>.
- Anczkiewicz, R., Oberli, F., Burg, J.P., Villa, I.M., Günther, D., Meier, M., 2001. Timing of normal faulting along the Indus Suture in Pakistan Himalaya and a case of major ^{231}Pa / ^{235}U initial disequilibrium in zircon. *Earth Planet. Sci. Lett.* 191, 101–114. [https://doi.org/10.1016/S0012-821X\(01\)00406-X](https://doi.org/10.1016/S0012-821X(01)00406-X).
- Andersen, T., 2002. Correction of common lead in U-Pb analyses that do not report ^{204}Pb . *Chem. Geol.* 192, 59–79.
- Andréasson, P.-G., Sverningsen, O., Johansson, I., Solyom, Z., Xiaodan, T., 1992. Mafic dyke swarms of the Baltica-Iapetus transition, Svea Nappe Complex of the Sarek Mts., Swedish Caledonides. *Geol. Föreningen i Stock. Förhandlingar* 114, 31–45.
- Barnes, C.J., Jeanneret, P., Kullerød, K., Majka, J., Schneider, D.A., Bukala, M., Klonowska, I., 2020a. Exhumation of the high-pressure Tsäkkok Lens, Swedish Caledonides: insights from the structural and white mica $^{40}\text{Ar}/^{39}\text{Ar}$ geochronological record. *Tectonics* 39, 1–23. <https://doi.org/10.1029/2020TC006242>.
- Barnes, C.J., Walczak, K., Janots, E., Schneider, D., Majka, J., 2020b. Timing of Paleozoic exhumation and deformation of the high-pressure Vestgötabyen complex at the Motalafjella Nunatak, Svalbard, in: Majka, J., Klonowska, I. (Eds.), *High and Ultra-High Pressure Rocks*. *Minerals* 10 (2), 1–23. <https://doi.org/10.3390/min10020125>.
- Bea, F., Montero, P., 1999. Behavior of accessory phases and redistribution of Zr, REE, Y, Th, and U during metamorphism and partial melting of metapelites in the lower crust: an example from the Kinzigite Formation of Ivrea-Verbano, NW Italy. *Geochim. Cosmochim. Acta* 63, 1133–1153.
- Budzyń, B., Sláma, J., Corfu, F., Crowley, J., Schmitz, M., Williams, M.L., Jercinovic, M. J., Kozub-Budzyń, G.A., Konečný, P., Rzepa, G., Włodek, A., 2021. TS-Mnz – a new monazite age reference material for U-Th-Pb microanalysis. *Chem. Geol.* 572, 120195. <https://doi.org/10.1016/j.chemgeo.2021.120195>.
- Buick, I.S., Allen, C., Pandit, M., Rubatto, D., Hermann, J., 2006. The Proterozoic magmatic and metamorphic history of the Banded Gneiss Complex, central Rajasthan, India: LA-ICP-MS U-Pb zircon constraints. *Precambrian Res.* 151, 119–142. <https://doi.org/10.1016/j.precamres.2006.08.006>.
- Bukala, M., Klonowska, I., Barnes, C., Majka, J., Kościńska, K., Janák, M., Fassmer, K., Broman, C., Luptáková, J., 2018. UHP metamorphism recorded by phengite eclogite from the Caledonides of northern Sweden: P-T path and tectonic implications. *J. Metamorph. Geol.* 36, 547–566. <https://doi.org/10.1111/jmg.12306>.
- Bukala, M., Barnes, C., Jeanneret, P., Hidas, K., Mazur, S., Almqvist, B.S.G., Kościńska, K., Klonowska, I., Surka, J., Majka, J., 2020. Brittle deformation during eclogitization or early Paleozoic blueschist, in: Biswal, T.K., Grasemann, B., Oriolo, S. (Eds.), *Meso- and Microscopic Structures: Implications for Tectonics*. *Front. Earth Sci.* 8, 594453. <https://doi.org/10.3389/feart.2020.594453>.
- Catlos, E.J., Miller, N.R., 2016. Ion microprobe ^{208}Th - ^{208}Pb ages from high common Pb monazite, Morefield Mine, Amelia County, Virginia: implications for Alleghanian tectonics. *Am. J. Sci.* 316, 470–503. <https://doi.org/10.2475/05.2016.03>.
- Catlos, E.J., Gilley, L.D., Harrison, T.M., 2002. Interpretation of monazite ages obtained via in situ analysis. *Chem. Geol.* 188, 193–215.
- Cherniak, D.J., Watson, E.B., Grove, M., Harrison, T.M., 2004. Pb diffusion in monazite: a combined RBS/SIMS study. *Geochim. Cosmochim. Acta* 68, 829–840. <https://doi.org/10.1016/j.gca.2003.07.012>.
- Copeland, P., Parrish, R.R., Harrison, T.M., 1988. Identification of inherited radiogenic Pb in monazite and its implications for U-Pb systematics. *Nature* 333, 760–763.
- Corfu, F., 2013. A century of U-Pb geochronology: the long quest towards concordance. *Bull. Geol. Soc. Am.* 125, 33–47. <https://doi.org/10.1130/B30698.1>.
- Didier, A., Bosse, V., Boulvais, P., Boulton, J., Paquette, J.-L., Montel, J.M., Devidal, J.-L., 2013. Disturbance versus preservation of U-Th-Pb ages in monazite during fluid – rock interaction: textural, chemical and isotopic in situ study in microgranites (Velay Dome, France). *Contrib. Miner. Petrol.* 165, 1051–1072. <https://doi.org/10.1007/s00410-012-0847-0>.
- Dubosq, R., Rogowitz, A., Schneider, D.A., Schweinar, K., Gault, B., 2021. Fluid inclusion induced hardening: nanoscale evidence from naturally deformed pyrite. *Contrib. Miner. Petrol.* 176, 15. <https://doi.org/10.1007/s00410-021-01774-9>.
- Engi, M., 2017. Petrochronology based on REE-minerals: Monazite, allanite, xenotime, apatite. In: Kohn, M.J., Engi, M., Lanari, P. (Eds.), *Petrochronology: Methods and Applications, Reviews in Mineralogy and Petrology*, 83, pp. 365–408. <https://doi.org/10.2138/rmg.2017.83.12>.
- Erickson, T.M., Pearce, M.A., Taylor, R.J.M., Timms, N.E., Clark, C., Reddy, S.M., Buick, I.S., 2015. Deformed monazite yields high-temperature tectonic ages. *Geology* 43 (5), 383–386. <https://doi.org/10.1130/G36533.1>.
- Fassmer, K., Froitzheim, N., Janák, M., Strohmeier, M., Bukala, M., Lagos, M., Munker, C., 2021. Diachronous collision in the Svea Nappe Complex: evidence from Lu-Hf geochronology of eclogites (Norrbottnen, North Sweden). *J. Metamorph. Geol.* <https://doi.org/10.1111/jmg.12591>.
- Ferry, J.M., Watson, E.B., 2007. New thermodynamic models and revised calibrations for the Ti-in-zircon and Zr-in-rutile thermometers. *Contrib. Miner. Petrol.* 154, 429–437. <https://doi.org/10.1007/s00410-007-0201-0>.
- Finger, F., Krenn, E., 2007. Three metamorphic monazite generations in a high-pressure rock from the Bohemian Massif and the potentially important role of apatite in stimulating polyphase monazite growth along a PT loop. *Lithos* 95, 103–115. <https://doi.org/10.1016/j.lithos.2006.06.003>.
- Fougerouse, D., Reddy, S.M., Saxey, D.W., Erickson, T.M., Kirkland, C.L., Rickard, W.D. A., Seydoux-Guillaume, A.-M., Clark, C., Buick, I.S., 2018. Nanoscale distribution of Pb in monazite revealed by atom probe microscopy. *Chem. Geol.* 479, 251–258. <https://doi.org/10.1016/j.chemgeo.2018.01.020>.
- Fougerouse, D., Reddy, S.M., Seydoux-Guillaume, A.M., Kirkland, C.L., Erickson, T.M., Saxey, D.W., Rickard, W.D.A., Jacob, D., Leroux, H., Clark, C., 2021. Mechanical twinning of monazite expels radiogenic lead. *Geology* 49, 417–421. <https://doi.org/10.1130/G48400.1>.
- Gee, D.G., Fossen, H., Henriksen, N., Higgins, A.K., 2008. From the Early Paleozoic Platforms of Baltica and Laurentia to the Caledonide Orogen of Scandinavia and Greenland. *Episodes* 31, 44–51.
- Gee, D.G., Klonowska, I., Andréasson, P.-G., Stephens, M.B., 2020. Middle thrust sheets in the Caledonide orogen, Sweden: The outer margin of Baltica, the continent-ocean transition zone and late Cambrian-Ordovician subduction-accretion. In: Stephens, M. B., Wiehede, J.B. (Eds.), *Sweden: Lithotectonic Framework, Tectonic Evolution and Mineral Resources*, Geological Society, London, Memoirs, pp. 517–548.
- Gonçalves, G.O., Lana, C., Scholz, R., Buick, I.S., Gerdes, A., Kamo, S.L., Marinho, M.M., Chaves, A.O., Valeriano, C., Arias, H., Júnior, N., 2016. An assessment of monazite from the Itambé pegmatite district for use as U-Pb isotope reference material for microanalysis and implications for the origin of the “Moacyr” monazite. *Chem. Geol.* 424, 30–50. <https://doi.org/10.1016/j.chemgeo.2015.12.019>.
- Grand’Homme, A., Janots, E., Seydoux-Guillaume, A.M., Guillaume, D., Bosse, V., Magnin, V., 2016. Partial resetting of the U-Th-Pb systems in experimentally altered monazite: nanoscale evidence of incomplete replacement. *Geology* 44, 431–434. <https://doi.org/10.1130/G37770.1>.
- Harlov, D.E., Förster, H.-J., 2003. Fluid-induced nucleation of (Y+REE)-phosphate minerals within apatite: nature and experiment. Part II. Fluorapatite. *Am. Miner.* 88, 1209–1229.
- Harlov, D.E., Wirth, R., Förster, H.-J., 2005. An experimental study of dissolution-reprecipitation in fluorapatite: fluid infiltration and the formation of monazite. *Contrib. Miner. Petrol.* 150, 268–286. <https://doi.org/10.1007/s00410-005-0017-8>.
- Holder, R.M., Hacker, B.R., Kylander-Clark, A.R.C., Cottle, J.M., 2015. Monazite trace-element and isotopic signatures of (ultra) high-pressure metamorphism: examples from the Western Gneiss Region, Norway. *Chem. Geol.* 409, 99–111. <https://doi.org/10.1016/j.chemgeo.2015.04.021>.
- Jakob, J., Andersen, T.B., Kjell, H.J., 2019. A review and reinterpretation of the architecture of the South and South-Central Scandinavian Caledonides—a magma-poor to magma-rich transition and the significance of the reactivation of rift inherited structures. *Earth-Sci. Rev.* 192, 513–528. <https://doi.org/10.1016/j.earscirev.2019.01.004>.
- Janots, E., Engi, M., Berger, A., Allaz, J., Schwarz, J.-O., Spandler, C., 2008. Prograde metamorphic sequence of REE minerals in pelitic rocks of the Central Alps: implications for allanite-monazite-xenotime phase relations from 250 to 610°C. *J. Metamorph. Geol.* 26, 509–526. <https://doi.org/10.1111/j.1525-1314.2008.00774.x>.
- Janots, E., Berger, A., Gnoss, E., Whitehouse, M., Lewin, E., Pettke, T., 2012. Constraints on fluid evolution during metamorphism from U-Th-Pb systematics in Alpine hydrothermal monazite. *Chem. Geol.* 326–327, 61–71. <https://doi.org/10.1016/j.chemgeo.2012.07.014>.
- Jastrzebski, M., Żelazniewicz, A., Budzyń, B., Sláma, J., Konečný, P., 2020. Age constraints on the pre-Variscan and Variscan thermal events in the Kamieniec Zabkowiecki metamorphic belt (the fore-sudetic block, SW Poland). *Ann. Soc. Geol. Pol.* 90, 27–49. <https://doi.org/10.14241/asgp.2020.05>.
- Jeanneret, P., Gonçalves, P., Durand, C., Trap, P., Marquer, D., Quirt, D., Ledru, P., 2017. Geochronological constraints on the trans-Hudsonian tectono-metamorphic evolution of the pre-Athabasca basement within the Wollaston-Mudjatik Transition Zone, Saskatchewan. *Precambrian Res.* 301, 152–178. <https://doi.org/10.1139/cjes-2015-0136>.
- Jonsson, E., Harlov, D.E., Majka, J., Högdahl, K., Persson-Nilsson, K., 2016. Fluorapatite-monazite-allanite relations in the Grängesberg apatite-iron oxide ore district, Bergslagen, Sweden. *Am. Miner.* 101, 1769–1782.
- Kamber, B.S., Moorbach, S., 1998. Initial Pb of the Amitsoq gneiss revisited: implication for the timing of early Archaean crustal evolution in West Greenland. *Chem. Geol.* 150, 19–41. [https://doi.org/10.1016/S0009-2541\(98\)00059-X](https://doi.org/10.1016/S0009-2541(98)00059-X).
- Kempe, U., Lehmann, B., Wolf, D., Rodionov, N., Bombach, K., Schwengfelder, U., Dietrich, A., 2008. U-Pb SHRIMP geochronology of Th-poor, hydrothermal monazite: an example from the Llallagua tin-porphyry deposit, Bolivia. *Geochimica Cosmochim. Acta* 72, 4352–4366. <https://doi.org/10.1016/j.gca.2008.05.059>.

- Kirkland, C.L., Erickson, T.M., Johnson, T.E., Danišik, M., Evans, N.J., Bourdet, J., McDonald, B.J., 2016. Discriminating prolonged, episodic or disturbed monazite age spectra: an example from the Kalak Nappe Complex, Arctic Norway. *Chem. Geol.* 424, 96–110. <https://doi.org/10.1016/j.chemgeo.2016.01.009>.
- Kjøll, H.J., 2020. Late Neoproterozoic basin evolution of the magma-rich Iapetus margin of Baltica. *Nor. J. Geol.* 100, 202005. <https://doi.org/10.17850/njg100-1-6>.
- Kohn, M.J., 2020. A refined zirconium-in-rutile thermometer. *Am. Miner.* 105, 963–971. <https://doi.org/10.2138/am-2020-7091>.
- Kohn, M.J., Vervoort, J.D., 2008. U-Th-Pb dating of monazite by single-collector ICP-MS: pitfalls and potential. *Geochemistry, Geophys. Geosystems* 9, 1–16. <https://doi.org/10.1029/2007GC001899>.
- Kohn, M.J., Wieland, M.S., Parkinson, C.D., Upreti, B.N., 2005. Five generations of monazite in Langtang gneisses: implications for chronology of the Himalayan metamorphic core. *J. Metamorph. Geol.* 23, 399–406. <https://doi.org/10.1111/j.1525-1314.2005.00584.x>.
- Konečný, P., Kusiak, M.A., Dunkley, D.J., 2018. Improving U-Th-Pb electron microprobe dating using monazite age references. *Chem. Geol.* 484, 22–35. <https://doi.org/10.1016/j.chemgeo.2018.02.014>.
- Kooijman, E., Smit, M.A., Ratschbacher, L., Kylander-Clark, A.R.C., 2017. A view into crustal evolution at mantle depths. *Earth Planet. Sci. Lett.* 465, 59–69. <https://doi.org/10.1016/j.epsl.2017.02.032>.
- Kornelussen, A., McLimans, R., Braathen, A., Erambert, M., Lutro, O., Ragnhildstveit, J., 2000. Rutile in eclogites as mineral resource in the Sunnfjord Region, western Norway. *NGU Bull.* 436, 39–47.
- Kramers, J.D., Tolstikhin, I.N., 1997. Two terrestrial lead isotope paradoxes, forward transport modelling, core formation and the history of the continental crust. *Chem. Geol.* 139, 75–110. [https://doi.org/10.1016/S0009-2541\(97\)00027-2](https://doi.org/10.1016/S0009-2541(97)00027-2).
- Krenn, E., Finger, F., 2004. Metamorphic formation of Sr-apatite and Sr-bearing monazite in a high-pressure rock from the Bohemian Massif. *Am. Miner.* 89, 1323–1329.
- Krenn, E., Putz, H., Finger, F., Paar, W.H., 2011. Sulfur-rich monazite with high common Pb in ore-bearing schists from the Schellgaden mining district (Tauern Window, Eastern Alps). *Miner. Petrol.* 102. <https://doi.org/10.1007/s00710-011-0170-x>.
- Kullerød, K., 1987. Origin and Tectonometamorphic Evolution of the Eclogites in the Tsäkkok Lens (Seve Nappes), Southern Norrbotten, Sweden. Candidate Scientific Thesis. University of Oslo, Oslo, Norway.
- Lanari, P., Vidal, O., De Andrade, V., Dubacq, B., Lewin, E., Grosch, E.G., Schwartz, S., 2014. Computers & Geosciences XMapTools: a MATLAB®-based program for electron microprobe X-ray image processing and geothermobarometry. *Comput. Geosci.* 62, 227–240.
- Majka, J., Be'eri-Shlevin, Y., Gee, D.G., Ladenberger, A., Claesson, S., Konečný, P., Klonowska, I., 2012. Multiple monazite growth in the Åreskutan migmatite: evidence for a polymetamorphic Late Ordovician to Late Silurian evolution in the Seve Nappe Complex of west-central Jämtland, Sweden. *J. Geosci.* 57, 3–23. <https://doi.org/10.3190/jgeosci.112>.
- McFarlane, C.R.M., Harrison, T.M., 2006. Pb-diffusion in monazite: Constraints from a high-T contact aureole setting. *Earth Planet. Sci. Lett.* 250, 376–384. <https://doi.org/10.1016/j.epsl.2006.06.050>.
- Meldrum, A., Boatner, L.A., Weber, W.J., Ewing, R.C., 1998. Radiation damage in zircon and monazite. *Geochim. Cosmochim. Acta* 62, 2509–2520. [https://doi.org/10.1016/S0016-7037\(98\)00174-4](https://doi.org/10.1016/S0016-7037(98)00174-4).
- Mohammadi, N., McFarlane, C.R.M., Lentz, D.R., 2019. U-Pb geochronology of hydrothermal monazite from uraniferous greisen veins associated with the high heat production, Mount Douglas Granite, New Brunswick, Canada. *Geosciences* 9, 224. <https://doi.org/10.3390/geosciences9050224>.
- Montel, J.-M., Foret, S., Veschambre, M., Nicollet, C., Provort, A., 1996. Electron microprobe dating of monazite. *Chem. Geol.* 131, 37–53. [https://doi.org/10.1016/0009-2541\(96\)00024-1](https://doi.org/10.1016/0009-2541(96)00024-1).
- Moussallam, Y., Schneider, D.A., Janák, M., Thöni, M., Holm, D.K., 2012. Heterogeneous extrusion and exhumation of deep-crustal Variscan assembly: geochronology of the Western Tatra Mountains, northern Slovakia. *Lithos* 144–145, 88–108. <https://doi.org/10.1016/j.lithos.2012.03.025>.
- Nasdale, L., Akhmaliev, S., Artac, A., Chanmuang, N.C., Habler, G., Lenz, C., 2018. Irradiation effects in monazite-(Ce) and zircon: Raman and photoluminescence study of Au-irradiated FIB foils. *Phys. Chem. Miner.* 45, 855–871. <https://doi.org/10.1007/s00269-018-0975-9>.
- Nasdale, L., Akhmaliev, S., Burakov, B.E., Chanmuang, N.C., Škoda, R., 2020. The absence of metamictisation in natural monazite. *Sci. Rep.* 10, 14676. <https://doi.org/10.1038/s41598-020-71451-7>.
- Paquette, J.L., Tiepolo, M., 2007. High resolution (5 µm) U-Th-Pb isotope dating of monazite with excimer laser ablation (ELA)-ICPMS. *Chem. Geol.* 240, 222–237. <https://doi.org/10.1016/j.chemgeo.2007.02.014>.
- Parrish, R.R., 1990. U-Pb dating of monazite and its application to geological problems. *Can. J. Earth Sci.* 27, 1431–1450. <https://doi.org/10.1139/e90-152>.
- Paton, C., Hellstrom, J., Paul, B., Woodhead, J., Hergt, J., 2011. Iolite: Freeware for the visualisation and processing of mass spectrometric. *J. Anal. At. Spectrom.* 26, 2508–2518. <https://doi.org/10.1039/C1JA10172B>.
- Petrus, J.A., Kamber, B.S., 2012. VizualAge: a novel approach to laser ablation ICP-MS U-Pb geochronology data reduction. *Geostand. Geoanal. Res.* 36, 247–270. <https://doi.org/10.1111/j.1751-908X.2012.00158.x>.
- Pyle, J.M., Spear, F.S., 2003a. Four generations of accessory-phase growth in low-pressure migmatites from SW New Hampshire. *Am. Mineral.* 88, 338–351.
- Pyle, J.M., Spear, F.S., 2003b. Yttrium zoning in garnet: coupling of major and accessory phases during metamorphic reactions. *Am. Mineral.* 88, 708.
- Pyle, J.M., Spear, F.S., Rudnick, R.L., McDonough, W.F., 2001. Monazite-xenotime-garnet equilibrium in metapelites and a new monazite-garnet thermometer. *J. Petrol.* 42, 2083–2107.
- Raison, P.E., Jardin, R., Bouëxière, D., Konings, R.J.M., Geisler, T., Pavel, C.C., Rebizant, J., Popa, K., 2008. Structural investigation of the synthetic CaAn (PO₄)₂ (An = Th and Np) cheralite-like phosphates. *Phys. Chem. Miner.* 35, 603–609. <https://doi.org/10.1007/s00269-008-0252-4>.
- Raison, P.E., Heathman, S., Wallez, G., Zvoriste, C.E., Bykov, D., Ménard, G., Suard, E., Popa, K., Dacheux, N., Konings, R.J.M., Caciuffo, R., 2012. Structure and nuclear density distribution in the cheralite-CaTh(PO₄)₂: Studies of its behaviour under high pressure (36 GPa). *Phys. Chem. Miner.* 39, 685–692. <https://doi.org/10.1007/s00269-012-0522-z>.
- Rasmussen, B., Muhling, J.R., 2007. Monazite begets monazite: evidence for dissolution of detrital monazite and reprecipitation of syntectonic monazite during low-grade regional metamorphism. *Contrib. Miner. Petrol.* 154, 675–689. <https://doi.org/10.1007/s00410-007-0216-6>.
- Rasmussen, B., Muhling, J.R., 2009. Reactions destroying detrital monazite in greenschist-facies sandstones from the Witwatersrand basin, South Africa. *Chem. Geol.* 264, 311–327. <https://doi.org/10.1016/j.chemgeo.2009.03.017>.
- Romer, R.L., 2003. Alpha-recoil in U-Pb geochronology: effective sample size matters. *Contrib. Miner. Petrol.* 145, 481–491. <https://doi.org/10.1007/s00410-003-0463-0>.
- Root, D., Corfu, F., 2012. U-Pb geochronology of two discrete Ordovician high-pressure metamorphic events in the Seve Nappe Complex, Scandinavian Caledonides. *Contrib. Miner. Petrol.* 163, 769–788. <https://doi.org/10.1007/s00410-011-0698-0>.
- Ruschel, K., Nasdale, L., Kronz, A., Hanchar, J.M., Többs, D.M., Škoda, R., Finger, F., Möller, A., 2012. A Raman spectroscopic study on the structural disorder of monazite-(Ce). *Mineral. Petrol.* 105, 41–55. <https://doi.org/10.1007/s00710-012-0197-7>.
- Schärer, U., 1984. The effect of initial 230Th disequilibrium on young U-Pb ages: the Makalu case, Himalaya. *Earth Planet. Sci. Lett.* 67, 191–204. [https://doi.org/10.1016/0012-821X\(84\)90172-9](https://doi.org/10.1016/0012-821X(84)90172-9).
- Schneider, D.A., Edwards, M.A., Kidd, W.S.F., Zeitler, P.K., Coath, C.D., 1999. Early Miocene anatexis identified in the western syntaxis, Pakistan Himalaya. *Earth Planet. Sci. Lett.* 167, 121–129. [https://doi.org/10.1016/S0012-821X\(99\)00022-9](https://doi.org/10.1016/S0012-821X(99)00022-9).
- Schoene, B., 2014. U-Th-Pb Geochronology. In: Holland, H.D., Turekian, K.K. (Eds.), *Treatise on Geochemistry*. Elsevier Publishing, pp. 341–378.
- Seydoux-Guillaume, A.-M., Wirth, R., Heinrich, W., Montel, J.-M., 2002. Experimental determination of Thorium partitioning between monazite and xenotime using analytical electron microscopy and X-ray diffraction Rietveld analysis. *Eur. J. Mineral.* 14, 869–878. <https://doi.org/10.1127/0935-1221/2002/0014-0869>.
- Seydoux-Guillaume, A.M., Goncalves, P., Wirth, R., Deutsch, A., 2003. Transmission electron microscope study of polyphase and discordant monazites: site-specific specimen preparation using the focused ion beam technique. *Geology* 31, 973–976. <https://doi.org/10.1130/G19582.1>.
- Seydoux-Guillaume, A.-M., Montel, J.-M., Bingen, B., Bosse, V., de Parseval, P., Paquette, J.-L., Janots, E., Wirth, R., 2012. Low-temperature alteration of monazite: fluid mediated coupled dissolution-precipitation, irradiation damage, and disturbance of the U-Pb and Th-Pb chronometers. *Chem. Geol.* 330–331, 140–158. <https://doi.org/10.1016/j.chemgeo.2012.07.031>.
- Seydoux-Guillaume, A.-M., Deschanel, X., Baumber, C., Neumeier, S., Weber, W.J., Peugot, S., 2018a. Why natural monazite never becomes amorphous: experimental evidence for alpha self-healing. *Am. Mineral.* 103, 824–827. <https://doi.org/10.2138/am-2018-6447>.
- Seydoux-Guillaume, A.M., Bingen, B., Bosse, V., Janots, E., Laurent, A.T., 2018b. Transmission electron microscope imaging sharpens geochronological interpretation of zircon and monazite. In: Moser, D., Corfu, F., Reddy, S.M., Darling, J., Tait, K. (Eds.), *Microstructural Geochronology: Planetary Records Down to Atom Scale*. John Wiley & Sons, Inc., pp. 261–275. <https://doi.org/10.1002/9781119227250.ch12>.
- Seydoux-Guillaume, A.-M., Fougereuse, D., Laurent, A.T., Gardès, E., Reddy, S.M., Saxey, D.W., 2019. Nanoscale resetting of the Th/Pb system in an isotopically-closed monazite grain: a combined atom probe and transmission electron microscopy study. *Geosci. Front.* 10, 65–76. <https://doi.org/10.1016/j.gsf.2018.09.004>.
- Skippton, D.R., Schneider, D.A., McFarlane, C.R.M., St-Onge, M.R., Jackson, S.E., 2016. Multi-stage zircon and monazite growth revealed by depth profiling and in situ U-Pb geochronology: Resolving the Paleoproterozoic tectonics of the Trans-Hudson Orogen on southeastern Baffin Island, Canada. *Precambrian Res.* 285, 272–298. <https://doi.org/10.1016/j.precamres.2016.09.002>.
- Skrzypek, E., Bosse, V., Kawakami, T., Martelat, J.E., Štípská, P., 2017. Transient allanite replacement and prograde to retrograde monazite (re)crystallization in medium-grade metasedimentary rocks from the Orlica-Sniežnik Dome (Czech Republic/Poland): textural and geochronological arguments. *Chem. Geol.* 449, 41–57. <https://doi.org/10.1016/j.chemgeo.2016.11.033>.
- Snijders, R., 1987. Structural Geology and Metamorphic Petrology of Metasedimentary Rocks in the Tsäkkok Lens (Seve Nappes) and in the Lower Koli Volcanosedimentary Rocks, Southern Norrbotten Caledonides, Sweden. Candidate Scientific Thesis. University of Oslo, Oslo, Norway.
- Spear, F.S., Pyle, J.M., 2010. Theoretical modeling of monazite growth in a low-Ca metapelite. *Chem. Geol.* 273, 111–119. <https://doi.org/10.1016/j.chemgeo.2010.02.016>.
- Spear, F.S., Pyle, J.M., Cherniak, D., 2009. Limitations of chemical dating of monazite. *Chem. Geol.* 266, 227–239. <https://doi.org/10.1016/j.chemgeo.2009.06.007>.
- Su, W., Li, J., Mao, Q., Gao, J., Liu, X., Chen, F., Ge, X.-M., 2018. Rutile in HP rocks from the Western Tianshan, China: mineralogy and its economic implications. *J. Earth Sci.* 29, 1049–1059.

- Suzuki, K., Kato, T., 2008. CHIME dating of monazite, xenotime, zircon and polycrase: Protocol, pitfalls and chemical criterion of possibly discordant age data. *Gondwana Res.* 14, 569–586. <https://doi.org/10.1016/j.gr.2008.01.005>.
- Suzuki, K., Adachi, M., Tanaka, T., 1991. Middle Precambrian provenance of Jurassic sandstone in the Mino Terrane, Central Japan: Th-U-total Pb evidence from an electron microprobe monazite study. *Sediment. Geol.* 75, 141–147.
- Szopa, K., Kusiak, M.A., Gawęda, A., Banasik, K., Chew, D., Dunkley, D.J., Iizuka, T., Janeczek, J., Konečný, P., Krzykowski, T., Yi, K., 2017. Monazite-(Ce) from the Skalna Brama Pegmatite, Sudety Mts, Poland, as potentially new reference material for U-Pb geochronology. *NGF Abstr. Proc.* 2.
- Tao, R., Zhang, L., Fei, Y., Liu, Q., 2014. The effect of Fe on the stability of dolomite at high pressure: Experimental study and petrological observation in eclogite from southwestern Tianshan, China. *Geochemica Cosmochim. Acta* 143, 253–267. <https://doi.org/10.1016/j.gca.2014.02.031>.
- Vermeesch, P., 2018. Geoscience Frontiers IsoplotR: a free and open toolbox for geochronology. *Geosci. Front.* 9, 1479–1493. <https://doi.org/10.1016/j.gsf.2018.04.001>.
- Vermeesch, P., 2020. Unifying the U–Pb and Th–Pb methods: joint isochron regression and common Pb correction. *Geochronology* 2, 119–131. <https://doi.org/10.5194/gchron-2-119-2020>.
- Wawrenitz, N., Krohe, A., Rhede, D., Romer, R.L., 2012. Dating rock deformation with monazite: the impact of dissolution precipitation creep. *Lithos* 134–135, 52–74. <https://doi.org/10.1016/j.lithos.2011.11.025>.
- Williams, M.L., Jercinovic, M.J., Hetherington, C.J., 2007. Microprobe monazite geochronology: understanding geologic processes by integrating composition and chronology. *Annu. Rev. Earth Planet. Sci.* 35, 137–175. <https://doi.org/10.1146/annurev.earth.35.031306.140228>.
- Williams, M.L., Jercinovic, M.J., Harlov, D.E., Budzyn, B., Hetherington, C.J., 2011. Resetting monazite ages during fluid-related alteration. *Chem. Geol.* 283, 218–225. <https://doi.org/10.1016/j.chemgeo.2011.01.019>.
- Williams, M.L., Jercinovic, M.J., Mahan, K.H., Dumond, G., 2017. Electron microprobe petrochronology. In: Kohn, M.J., Engi, M., Lanari, P. (Eds.), *Petrochronology: Methods and Applications, Reviews in Mineralogy and Petrology*, 83, pp. 153–182. <https://doi.org/10.2138/rmg.2017.83.5>.
- Yan, T., Liu, D., Si, C., Qiao, Y., 2020. Coupled U-Pb Geochronology of monazite and zircon for the Bozhushan Batholith, Southeast Yunnan Province, China: Implications for regional metallogeny. *Minerals* 10, 239.
- Zack, T., Kooijman, E., 2017. Petrology and Geochronology of Rutile. In: Kohn, M.J., Engi, M., Lanari, P. (Eds.), *Petrochronology: Methods and Applications, Reviews in Mineralogy and Petrology*, 83, pp. 443–467. <https://doi.org/10.2138/rmg.2017.83.14>.
- Zack, T., Moraes, R., Kronz, A., 2004. Temperature dependence of Zr in rutile: empirical calibration of a rutile thermometer. *Contrib. Miner. Petrol.* 148, 471–488. <https://doi.org/10.1007/s00410-004-0617-8>.